

Twin Tests Book of Reference

Twin Test 4: Scale Effects in Urban Flows

Lead Beneficiary: KIT
Dissemination Level: Public

Authors: Nikolaos-Petros Pallas, Brian Dsouza, V.
Pappa, J. Prospathopoulos, P. Chasapogiannis,
C. Gromke, A. Sciacchitano, D. Bouris

WP4

Widening of technical capacity and competence

TWEET-IE / Twin Wind tunnels for Energy and the
EnvironmentT - Innovations and Excellence
HORIZON-WIDERA-2021-ACCESS-03-01 / PR# 101079125



Co-funded by
the European Union

Deliverable 4.1

Executive Summary

The present chapter of the book of references refers to the fourth twin test of the TWEET-IE project, carried out in the wind tunnels of the Technical University of Delft (TU Delft) and the National Technical University of Athens (NTUA), using measurement equipment mainly provided by TU Delft.

An investigation of the scale effects on flow in the urban environment is carried out. More specifically, this urban environment is a series of five consecutive street canyons perpendicular to the approaching flow, simulating the urban fabric, since the street canyon geometry is usually considered as a fundamental component of contemporary cities. The examined canyon was the fourth one with respect to the direction of the approaching flow. The effect of vegetation (hedges at the pedestrian level or roof greening) on the flow is also examined throughout this study. In the wind tunnel of the National Technical University of Athens, all the former cases were investigated for two different values of ambient turbulence intensity corresponding to two distinct experimental configurations (i.e. with and without a passive grid). The study at NTUA was performed with a 3D-3C Robotic Particle Tracking Velocimetry (3D-PTV) System and at TU Delft with a 3D-3C Volumetric PTV system. Both systems can be categorised as volumetric methods. Additionally, surface pressure measurements were conducted in both wind tunnels whereas hot-film anemometry was employed in NTUA's wind tunnel to supplement the PTV-extracted dataset.

The beginning of the report documents details of the measurement methods and practical advice resulting from their application during the experiments at the two wind tunnels. Results and analysis of the measurements are presented. Overall, qualitative trends regarding Reynolds-number-independence agree well between the two wind tunnels. Results are not quantitatively or, in some cases, even qualitatively identical, but their differences provide an opportunity to analyse the effects of the different wind tunnel (WT) configurations (i.e. closed-loop WT vs. open jet WT) on Reynolds-number sensitivity.

History and Changes

| Ver | Date | Description | Contributors |
|-----|------------|-------------|---------------------|
| 00 | 01/04/2025 | Report | NTUA, TU Delft, KIT |

Contents

| | |
|---|-----------|
| EXECUTIVE SUMMARY | 2 |
| HISTORY AND CHANGES | 3 |
| CONTENTS | 4 |
| LIST OF FIGURES..... | 6 |
| LIST OF TABLES | 9 |
| 1 INTRODUCTION | 10 |
| 2 NTUA - EQUIPMENT AND METHODS. APPLIED KNOWLEDGE. | 13 |
| 2.1 INTRODUCTION | 13 |
| 2.1.1 <i>The NTUA wind tunnel</i> | 13 |
| 2.2 PTV MEASUREMENTS..... | 14 |
| 2.2.1 <i>Introduction to PTV & comparison with PIV</i> | 14 |
| 2.2.2 <i>Components of the Robotic PTV system</i> | 15 |
| 2.2.2.1 Robotic Arm and Cameras | 15 |
| 2.2.2.2 Illumination | 16 |
| 2.2.2.3 Seeding | 17 |
| 2.2.3 <i>Calibration of the Robotic PTV system</i> | 17 |
| 2.2.3.1 Geometric Calibration..... | 17 |
| 2.2.3.2 Volumetric Self-Calibration..... | 18 |
| 2.2.4 <i>Processing of PTV raw data</i> | 19 |
| 2.3 COMPLEMENTARY MEASUREMENTS..... | 20 |
| 2.3.1 <i>Surface pressure measurements</i> | 20 |
| 2.3.2 <i>Hot-wire measurements</i> | 21 |
| 2.4 SAFETY INSTRUCTIONS..... | 23 |
| 2.5 MODEL PREPARATION | 23 |
| 2.6 REFERENCE VELOCITY AND BACKGROUND FLOW | 25 |
| 3 TU DELFT - EQUIPMENT AND METHODS. TRAINING AND DOCUMENTATION. | 29 |
| 3.1 INTRODUCTION | 29 |
| 3.1.1 <i>The TU Delft Open Jet Facility (OJF)</i> | 29 |
| 3.2 PTV MEASUREMENTS..... | 30 |
| 3.2.1 <i>Components of the PTV system</i> | 30 |
| 3.2.1.1 Cameras | 30 |
| 3.2.1.2 Illumination..... | 31 |
| 3.2.1.3 High-speed Controller | 31 |
| 3.2.1.4 Seeding | 32 |
| 3.2.2 <i>Calibration of PTV system</i> | 33 |
| 3.2.2.1 Intensity Calibration..... | 33 |
| 3.2.2.2 Geometric Calibration..... | 33 |
| 3.2.2.3 Volume Self-Calibration | 34 |
| 3.2.3 <i>Processing of PTV raw data</i> | 34 |
| 3.3 SURFACE PRESSURE MEASUREMENTS..... | 34 |
| 3.4 SAFETY INSTRUCTIONS..... | 34 |
| 3.5 MODEL PREPARATION | 34 |
| 3.6 REFERENCE VELOCITY | 35 |
| 4 RESULTS..... | 36 |
| 4.1 TEST MATRICES | 36 |
| 4.2 PTV UNCERTAINTY | 37 |

| | | |
|-------|---|----|
| 4.3 | SCALING EFFECTS | 39 |
| 4.3.1 | <i>Hot-wire measurements</i> | 39 |
| 4.3.2 | <i>Pressure measurements</i> | 40 |
| 4.3.3 | <i>PTV measurements</i> | 41 |
| 4.4 | EFFECTS OF VEGETATION | 51 |
| 4.5 | INFLUENCE OF FREE STREAM TURBULENCE | 54 |
| 4.5.1 | <i>Hot-wire measurements</i> | 54 |
| 4.5.2 | <i>PTV measurements</i> | 55 |
| 5 | REFERENCES | 58 |

List of figures

| | |
|---|----|
| Figure 1. Illustrative examples of: (a) seeding with HSFB (NTUA), (b) experimental setup (TU Delft) and (c) passive grid (NTUA)..... | 10 |
| Figure 2. Wind Tunnel layout..... | 13 |
| Figure 3. Experimental setup using the Coaxial Volumetric Velocimetry (CVV) probe mounted on a Universal Robots UR5 robotic arm at NTUA’s facilities..... | 15 |
| Figure 4. LED Flashlight 300..... | 16 |
| Figure 5. Calibration plate 395-54 SSSP used for geometric calibration..... | 18 |
| Figure 6. Schematic illustration of the position of the pressure taps relative to the examined canyon and the approaching flow..... | 20 |
| Figure 7. position of measured velocity profiles (red lines) for: (a) characterisation of the developed boundary layer on the roofs of the 3 rd , 4 th and 5 th building models. The geometric loci of the lines are also given in parentheses. (b) quantification of the approaching flow in front of the whole model. The same coordinate system applies to both figures..... | 22 |
| Figure 8. Geometric configuration of the building models and structural details..... | 24 |
| Figure 9. Schematic illustration of the position of vegetation with respect to the examined canyon along with the necessary dimensions..... | 25 |
| Figure 10. Profiles of the approaching flow at two different positions (see Figure 7b) i.e. $Y = 0$ and $Y = L/2$ for: (a) the time-average, non-dimensional velocity U/U_∞ and (b) the turbulence intensity u'^2/U where u' is the streamwise velocity fluctuation. The results pertain to the case without the passive grid (low ambient turbulence intensity)..... | 26 |
| Figure 11. Profiles of the approaching flow at two different positions (see Figure 7b) i.e. $Y = 0$ and $Y = L/2$ for: (a) the time-average, non-dimensional velocity U/U_∞ and (b) the turbulence intensity u'^2/U where u' is the streamwise velocity fluctuation. The results pertain to the case with the passive grid of Figure 1c (higher ambient turbulence intensity)..... | 26 |
| Figure 12. A comparison between the profiles along the lines L1($X = -0.5W, Y = 0, Z$), L2($X = 2.5W, Y = 0, Z$) and L3($X = -2.5W, Y = 0, Z$) (see Figure 7a) corresponding to the center of the roofs of the 4 th (green), 5 th (blue) and 3 rd (purple) building models, respectively. This comparison is made for: (a) the time-average, non-dimensional velocity and (b) the turbulence intensity. The Reynolds number is equal to 60000 and the passive grid of Figure 1c had been applied on the inlet of the test section (ambient turbulence intensity $\sim 5\%$)..... | 27 |
| Figure 13. A comparison between the profiles along the lines L1($X = -0.5W, Y = 0, Z$) and L2($X = 2.5W, Y = 0, Z$) (see Figure 7a) corresponding to the center of the roofs of the 4 th (green) and 5 th (blue) buildings, respectively. This comparison is made for: (a) the time-average, non-dimensional velocity and (b) the turbulence intensity. The passive grid was not applied on the inlet of the test section (ambient turbulence intensity $\sim 1\%$), and the Reynolds number is 60000..... | 28 |
| Figure 14. (a) schematic illustration of the open jet facility (adjusted from [23]) and (b) a photograph of the outlet of the open jet facility. The cameras as well as the small street canyon models can be also seen..... | 29 |
| Figure 15. (a) configuration of the cameras and (b) utilisation of a measuring tape as a reference during focusing of the cameras (small building models, [3])..... | 30 |
| Figure 16. The utilised Programmable Timing Unit (PTU-X) responsible for the synchronisation of cameras and the LED lights..... | 32 |
| Figure 17. Control pane of the Fluid Supply Unit (FSU)..... | 32 |
| Figure 18. Control panel for the automatic adjustment of the reference velocity..... | 35 |

Figure 19. Global uncertainty metric $\epsilon_{97.5\%}/U_{ref}$ (%) for the *low turb* and *high turb* configurations at NTUA and the basic configuration at TU Delft. The value of the latter metric is given for every available Re number.38

Figure 20. Uncertainty (ϵ/U_{ref}) profiles for the *low turb* NTUA configuration and the basic TU Delft one at $X/H = 0.5$ and $Y/H = 0$ i.e. the centre-line of the plane of symmetry.38

Figure 21. (a) Time-average non-dimensional (streamwise) velocity and (b) turbulence intensity profiles for 5 different Reynolds numbers in the range 25000, 60000, along the L1($X = -0.5W, Y = 0, Z$) line shown in Figure 7a (located at the center of the 4th building’s roof). The results pertain to the case with the passive grid of Figure 1c. Hot-wire measurements were performed only in the wind tunnel of NTUA.39

Figure 22. (a) Time-average non-dimensional (streamwise) velocity and (b) turbulence intensity profiles for 5 different Reynolds numbers in the range 25000, 60000, along the L1($X = -0.5W, Y = 0, Z$) line shown in Figure 7a (located at the center of the 4th building’s roof). The results pertain to the case without the passive grid. Hot-wire measurements were performed only in the wind tunnel of NTUA.40

Figure 23. Surface pressure coefficient profiles for different Reynolds numbers within the range: (a) [25000, 100000] (NTUA experiment) and (b) [30000, 100000] (TU Delft experiment).41

Figure 24. Velocity vectors (tangent) and contours of the normalised mean streamwise velocity component U/U_{ref} for: (a) $Re = 25000$ and (b) $Re = 60000$, in the centre-plane. The flow is from left to right, with $U_{ref} = U_{\infty}$42

Figure 25. Profiles of the non-dimensional: (a) mean streamwise velocity (U/U_{ref}), (b) mean vertical velocity (W/U_{ref}) and (c) turbulent kinetic energy (k/U_{ref}^2) for $Re \in [25000, 60000]$ at $X/H = 0.5$ and $Y/H = 0$, with $U_{ref} = U_{\infty}$43

Figure 26. Profiles of the non-dimensional: (a) mean vertical velocity (W/U_{ref}) and (b) turbulent kinetic energy (k/U_{ref}^2) for $Re \in [25000, 60000]$ at $X/H = 0.003$ (leeward wall) and $Y/H = 0$, with $U_{ref} = U_{\infty}$44

Figure 27. Profiles of the non-dimensional: (a) mean vertical velocity (W/U_{ref}) and (b) turbulent kinetic energy (k/U_{ref}^2) for $Re \in [25000, 60000]$ at $X/H = 0.98$ (windward wall) and $Y/H = 0$, with $U_{ref} = U_{\infty}$44

Figure 28. Velocity vectors (tangent) and contours of the normalised mean lateral velocity component V/U_{ref} for: (a) $Re = 25000$ and (b) $Re = 60000$, in the plane located at $Y/H = 3.5$ (half a canyon’s height/width away from the edge of the canyon). The flow is from left to right, with $U_{ref} = U_{\infty}$. Negative values of V/U_{ref} point inwards i.e. towards the central region of the canyon.45

Figure 29. Profiles of the non-dimensional: (a) mean streamwise velocity (U/U_{ref}), (b) mean vertical velocity (W/U_{ref}), (c) mean lateral velocity (V/U_{ref}) and (d) turbulent kinetic energy (k/U_{ref}^2) for $Re \in [25000, 60000]$ at $X/H = 0.5$ and $Y/H = 3.5$, with $U_{ref} = U_{\infty}$46

Figure 30. Velocity vectors (tangent) and contours of the normalised mean streamwise velocity component U/U_{ref} for: (a) $Re = 30000$ and (b) $Re = 100000$, in the centre-plane. The flow is from left to right, with $U_{ref} = U_{\infty}$47

Figure 31. Profiles of the non-dimensional: (a) mean streamwise velocity (U/U_{ref}), (b) mean vertical velocity (W/U_{ref}) and (c) turbulent kinetic energy (k/U_{ref}^2) for $Re \in [30000, 100000]$ at $X/H = 0.5$ and $Y/H = 0$, with $U_{ref} = U_{\infty}$48

Figure 32. Profiles of the non-dimensional: (a) mean vertical velocity (W/U_{ref}) and (b) turbulent kinetic energy (k/U_{ref}^2) for $Re \in [30000, 100000]$ at $X/H = 0.07$ and $Y/H = 0$, with $U_{ref} = U_{\infty}$49

Figure 33. Profiles of the non-dimensional: (a) mean vertical velocity (W/U_{ref}) and (b) turbulent kinetic energy (k/U_{ref}^2) for $Re \in [30000, 100000]$ at $X/H = 0.93$ and $Y/H = 0$, with $U_{ref} = U_{\infty}$.

.....49

Figure 34. Velocity vectors (tangent) and contours of the normalised mean lateral velocity component V/U_{ref} for: (a) $Re = 30000$ and (b) $Re = 100000$, in the plane located at $Y/H = 3.5$ (half a canyon’s height/width away from the edge of the canyon). The flow is from left to right, with $U_{ref} = U_{\infty}$. Negative values of V/U_{ref} point inwards i.e. towards the central region of the canyon.

.....50

Figure 35. Profiles of the non-dimensional: (a) mean streamwise velocity (U/U_{ref}), (b) mean vertical velocity (W/U_{ref}), (c) mean lateral velocity (V/U_{ref}) and (d) turbulent kinetic energy (k/U_{ref}^2) for $Re \in [30000, 100000]$ at $X/H = 0.5$ and $Y/H = 3.5$, with $U_{ref} = U_{\infty}$.

.....51

Figure 36. Velocity vectors (tangent) and contours of the normalised mean streamwise velocity component U/U_{ref} in the centre-plane ($Y/H = 0$) of the canyon, for the: (a) bare canyon case, (b) configuration with roof greening and (c) configuration with the hedge row where the latter is indicated by the red dashed box. The flow is from left to right and the Reynolds number is equal to 60000 for all cases, with $U_{ref} = U_{\infty}$.

.....52

Figure 37. Velocity vectors (tangent) and contours of the normalised mean lateral velocity component V/U_{ref} for the: (a) bare canyon case, (b) configuration with roof greening and (c) configuration with the hedge row (indicated by the black dashed box), in the plane located at $Y/H = 3.5$ (half a canyon’s height/width away from the edge of the canyon). The flow is from left to right and the Reynolds number is equal to 60000 for all cases, with $U_{ref} = U_{\infty}$. Negative values of V/U_{ref} point inwards i.e. towards the central region of the canyon.

.....53

Figure 38. (a) Time-average non-dimensional (streamwise) velocity and (b) turbulence intensity profiles along the L1($X = -0.5W, Y = 0, Z$) line shown in Figure 7a (located at the center of the 4th building’s roof). The black curves correspond to the case with the passive grid while the red ones to the case without it. The Reynolds number is equal to 60000. Hot-wire measurements were performed only in the wind tunnel of NTUA.

.....54

Figure 39. (a) Time-average non-dimensional velocity and (b) turbulence intensity profiles along the L2($X = 2.5W, Y = 0, Z$) line shown in Figure 7a (located at the center of the 5th building’s roof). The black curves correspond to the case with the passive grid while the red ones to the case without it. The Reynolds number is equal to 60000. Hot-wire measurements were performed only in the wind tunnel of NTUA.

.....55

Figure 40. Velocity vectors (tangent) and contours of the normalised mean streamwise velocity component U/U_{ref} in the centre-plane ($Y/H = 0$) of the canyon, for the: (a) low turbulence case (without the passive grid), (b) high turbulence case (with the passive grid). The flow is from left to right and the Reynolds number is equal to 60000 for both figures, with $U_{ref} = U_{\infty}$.

.....56

Figure 41. Profiles of the non-dimensional: (a) mean streamwise velocity (U/U_{ref}), (b) mean vertical velocity (W/U_{ref}) and (c) turbulent kinetic energy (k/U_{ref}^2) for the low and high (dashed lines) turbulence cases at $X/H = 0.5$ and $Y/H = 0$, with $U_{ref} = U_{\infty}$. Results are shown for the minimum and maximum Reynolds numbers tested in the wind tunnel of NTUA i.e. 25000 and 60000.

.....57

List of tables

| | |
|---|----|
| Table 1. Focal length f (mm) of the employed lenses for all cameras in both scenarios (large and small models)..... | 31 |
| Table 2. $f\#$, magnification factor M and digital image resolution (pixel/mm) for all field of views in both scenarios (large and small models)..... | 31 |
| Table 3. Test matrix containing the individual experiments conducted in the open jet facility of TU Delft. The smaller canyon had an $h = 0.05$ m and the larger canyon, where greening was also tested, had $h = 0.15$ m..... | 36 |
| Table 4. Test matrix containing the individual experiments conducted in the wind tunnel facility of NTUA. | 37 |

1 Introduction

The scope of the experiments and methods presented in the present chapter is twofold:

1. In the framework of the TWEET-IE project, a twin test is performed. One wind tunnel (WT) testing campaign was performed in the wind tunnel of the National Technical University of Athens (NTUA), Greece, which has a closed test section, while another one was undertaken in the open jet facility of the Technical University of Delft (TU Delft), the Netherlands. The measurement equipment for both the experiments was provided by TU Delft.

The model setup was the same for the two tests: 5 consecutive street canyons (six building models) were inserted in the test section (NTUA or TU Delft) in order to simulate the urban fabric (“*urban roughness*”, [1]). These street canyons are perpendicular to the approaching flow. Robotic Particle Tracking Velocimetry (at NTUA) or Volumetric Particle Tracking Velocimetry (at TU Delft) measurements were conducted within and slightly around the 4th street canyon by making use of the same seeding i.e. Helium-filled soap bubbles (HFSB). An example of the density and the appearance of the seeding is given in Figure 1a, where the developed vortex in the examined canyon is visually discernible. More details regarding the geometry and the experimental setup will be given in the forthcoming sections. An illustrative example of the experimental setup at TU Delft is given in Figure 1b, where the building models, a calibration target (on top of the examined canyon) as well as two of the three utilised cameras can be seen. Note that the height-to-width (H/W) and the length-to-width (L/W) aspect ratios of the street canyons are 1 and 8, respectively (“*skimming flow*” regime, [2]) for both experiments.



(a)



(b)



(c)

Figure 1. Illustrative examples of: (a) seeding with HFSB (NTUA), (b) experimental setup (TU Delft) and (c) passive grid (NTUA).



The exact same foam material was used for the modelling of vegetation (when needed) in both experimental campaigns. The only additional element in the setup of NTUA's experiment is the use of a passive grid (Figure 1c), which increases the ambient turbulence intensity. This feature was only used in some cases. In the open jet facility (OJF) of the TU Delft, smaller (by a factor of 3) but geometrically similar models were also used, in order to achieve even lower Reynolds numbers ($Re \leq 30000$) since the lowest achievable wind speed was 3 m/s. These models had been already used in [3]. Vegetation was not tested for the small models.

Measurements of the velocity and turbulence intensity were performed using hot-wire anemometry in the wind tunnel of NTUA for documenting the developed boundary layer on top of the roofs of selected buildings (including those of the examined canyon). The aim was to obtain an understanding of the approaching flow. In the OJF of TU Delft, velocity and turbulence intensity measurements were conducted by using volumetric Particle Tracking Velocimetry (PTV). Also, average surface pressures are obtained where the centre-plane of the examined street canyon crosses the fourth building model. These measurements were performed in both facilities, in order to further examine scale effects on the developed flow. Measurement space overlaps among the two experiments and so comparison of the results is possible to identify, characterise and categorise important sources of deviations such as external conditions, testing equipment etc. between test data obtained at different wind tunnel facilities.

2. The tests are of significant research value in themselves as they examine scale effects of flows in the urban environment, which is a burning issue for wind tunnel testing in general. There is also significant interest in establishing Reynolds number independence criteria specifically for street canyons, as proven by recent attempts ([4], [5]). The requirement of having the same value of Reynolds number in the reduced scale as that of the full scale is most often unattainable with wind tunnel testing. For this reason, the determination of the Reynolds number range within which the flow can be considered as Reynolds-independent is crucial for the acquisition of accurate measurements. Furthermore, the utilisation of state-of-the-art experimental techniques, such as the ones employed here (robotic and volumetric particle tracking velocimetry) are expected to shed more light on this topic, since axiomatically, the more accurate is one experimental technique the more difficult is to satisfy Reynolds-independence. For example, time-averaged velocity data could satisfy Reynolds-independence while higher statistical moments could showcase different behaviour (e.g. [3]). Moreover, the employment of particle tracking velocimetry gives the opportunity for more detailed representation of the flow field, increasing the potential of more thorough and local inspection of the scale effects on the flow field.

Capturing 3-D phenomena near the edge of the examined street canyon and examining scale effects also on this part of the flow field is expected to provide information which is not readily available in the open literature. The same also applies for the extracted pressure measurements, since to the best of the authors' knowledge, this is the first time that the influence of the Reynolds number on surface pressures within a street canyon is examined, at least in an experimental framework. Finally, investigating the influence of vegetation, such



as roof greening or hedge rows, adds another piece to the puzzle, contributing to a more realistic/complicated scenario.

The current report presents the methods, materials, procedures and results of the twin tests carried out at NTUA and TU Delft. The level of detail is not intended to substitute manuals or equipment-specific information. It is rather a documentation of procedures followed, and experience gained through the tests, in order to:

- a) Facilitate cross comparison of the results.
- b) Facilitate assessment of sources of deviations among the “twin” tests, in order to ultimately improve procedures.
- c) Provide a starting point for users of the facilities.
- d) Provide a guide for researchers intending to perform similar tests with similar equipment.



2.2 PTV measurements

2.2.1 Introduction to PTV & comparison with PIV

The experimental setup of Particle Tracking Velocimetry (PTV) has a lot of similarities with that of Particle Image Velocimetry (PIV) since they essentially have the same working principle for the acquisition of raw data.

Particle Image Velocimetry (PIV) is based on the principle of optical tracking of particles, whose trajectories and velocities represent those of the fluid flow. Having started the fan of the wind tunnel and for the desired velocity, seeding particles are injected into the test section. To produce seeding particles, a system of compressed air may be required, consisting of a compressor and an appropriate tubing system leading the compressed air to the source of seeding. In the case where helium-filled soap bubbles (HFSB) are used, the soap as well as the helium should be under pressure and not only the air. An illumination source (high energy lasers or LEDs) as well as high-speed cameras are required. For the acquisition of 2-component (2C) velocity measurements on a specific plane (2D) of interest, only one high-speed camera is necessary (2D-2C PIV) while for 3-component (3C) planar (2D) velocity measurements two high-speed cameras are required, in order to obtain a perspective of depth (2D-3C or Stereo-PIV). For the undertaking of volumetric (3D) measurements, at least 3 high-speed cameras should be present to capture the 3-component velocity field in a desired volume (3D-3C or Tomo-PIV/PTV). In the present experiments, where volumetric measurements of the 3-component velocity field were obtained, at least 3 cameras were used. The Robotic PTV system that was used in NTUA's wind tunnel was equipped with 4 cameras mounted onto a robotic arm while in the OJF of TU Delft 3 high speed cameras, mounted on an appropriate beam, were utilised.

However, the following question arises: what is the difference between PIV and PTV? Processing of PIV data is based on cross-correlation of image intensity between interrogation windows/voxels (divisions of the measurement plane/volume, usually in the cartesian system) of two or more consecutive image recordings. Finally, according to the location of the peaks in the cross-correlation map, a statistical representation of the displacement of the particles inside each interrogation window is obtained. This cross-correlation map can then be used for the calculation of the velocity, since the separation time of the image recordings is known. In Tomo-PIV, tomographic reconstruction (3D object reconstruction, [6]) is applied before the subsequent step of cross-correlation, since three (or more) individual recordings are available from the three (or more) corresponding cameras at every instance. The image recordings are basically 2-D representations (image space) of the same measurement volume captured by different cameras and therefore a voxel-based reconstruction step is necessary for the representation of the full 3-D volume (real world space). An overview of the reconstruction techniques is given in [6] and [7].

In Particle Tracking Velocimetry the usage of cross-correlation is completely avoided. Instead of an approach where the measurement volume is divided into interrogation windows/voxels, with PTV the tracks of individual particles are sought. This is done by making use of the Shake-the-Box algorithm ([8], [9]) a particularly efficient and fast method based on image matching (i.e. minimisation of residuals between subsequent image recordings) and not on cross-correlation as in PIV. Furthermore, tomographic reconstruction is not usually necessary in PTV unless a hybrid method is employed. Once the 3D mapping function from the image planes to the real 3D volume is known through geometric calibration, each particle can be identified by triangulation, based on epipolar geometry. Finally, PTV can yield significantly higher spatial resolution since it is based on

tracking individual particles (at numbers of tens or even hundreds of thousands for each time step, [8]), and not on a statistical representation of particle displacement within an interrogation region. Note that the Shake-the-Box algorithm is based on a previously developed method called Iterative Particle Reconstruction [10] but it is extended to incorporate temporal information in order to predict particle positions at the next time step [8]. An Eulerian representation can be obtained from the Lagrangian particle tracks by applying binning [11] which consists of division of the measurement volume into bins and subsequent ensemble-averaging within each bin.

2.2.2 Components of the Robotic PTV system

2.2.2.1 Robotic Arm and Cameras

The Coaxial Volumetric Velocimetry (CVV) probe is mounted on a Universal Robots UR5 robotic arm with six degrees of freedom (3 rotations and 3 translations) and with the accuracy of the translation of the robotic arm being 0.1mm. RoboDK software is used to program positions of the CVV probe in order to capture images from different views. This probe consists of four CMOS cameras with focal length equal to 4mm which are enclosed in an aerodynamic shell (LaVision Minishaker Aero). For more details regarding the CVV probe the readers are referred to Table 1 and Figure 3 of [3] while for the working principles of CVV they are referred to [12]. A photograph of the experimental setup is given in Figure 3.



Figure 3. Experimental setup using the Coaxial Volumetric Velocimetry (CVV) probe mounted on a Universal Robots UR5 robotic arm at NTUA's facilities.

The value of the acquisition frequency was chosen depending on the different Reynolds numbers to ensure that an adequate number of vortex turnovers (located at the centre-plane) is captured. A value greater than 50 ($N_t > 50$) is usually considered adequate. Here we opted for a number ~ 80 -100. If U_∞ is the free-stream velocity, the following assumption is made [13]:

$$U_{SC} = 0.3U_{\infty} \quad (1)$$

where U_{SC} is the magnitude of the velocity inside the canyon, associated with the developed vortex. The time for one turnover of the vortex is calculated by the following equation:

$$T_t = \pi H / U_{SC} \quad (2)$$

with H being the height of the canyon (equal to the width W). So basically H is considered to be the “diameter” of the vortex.

Finally, the acquisition frequency, $f_{acq} = N/T_{acq}$ (where N is the number of the captured image recordings), is chosen as such so that the following equation holds:

$$aT_{acq}/T_t = N_t \approx 80 - 100 \quad (3)$$

where $a \in \mathbb{N}$ is a user-defined parameter determining the number of individual acquisitions to reach the desired number of vortex turnovers. Efforts were made to keep this parameter equal to 5 for most acquisitions with at least 3000 images captured per acquisition. The higher the value of the parameter a the lower are the RAM storage requirements during a single acquisition. This is determined by available computational resources. Note that the maximum acquisition frequency of this system is 727Hz. In any case, the total number of turnover times processed (i.e. independent samples) did not fall below $N_t = 60$.

2.2.2.2 Illumination

Two LaVision LED Flashlight 300s (Figure 4 and Figure 3) were utilised to obtain sufficient pulsed volumetric illumination. Each module consists of an array of 72 high-power LEDs in an area of 300x100mm². The incoherent white light provides high image quality with constant and homogeneous brightness in time and space. The LEDs have an operating angle of 10° and a maximum frequency of 20kHz while they can be used in continuous or pulsed mode.



Figure 4. LED Flashlight 300.

Non-reflective paint is often used in these configurations, to minimise the background light reflections within the field of view of the cameras. Selected building models as well as the floor of the examined canyon were painted with Musou Black paint, which can absorb 99.4% of light in the visible range [14]. Note that the coat of paint should be renewed regularly since it can come off because of extended exposure to the HFSB seeding.

2.2.2.3 Seeding

Neutrally buoyant helium-filled soap bubbles ([6], [15]) of 300 μm median diameter [16] were used as tracer particles for PTV. The relatively large size of the HFSB permits the use of LEDs instead of lasers since more light is scattered by this type of seeding than by more conventional seeding materials e.g. oil droplets (section 2.1.6 of [6]). The Fluid Supply Unit (FSU) controls the pressures of helium, air, and soap solution, which can be fine-tuned to adjust the approximate size and number of bubbles produced by the seeding rake. The seeding rake comprises 200 bubble generators arranged in 10 parallel wings of 1m each with the seeding surface being approximately $0.5 \times 0.95 \text{m}^2$. During the measurements, the pressures were kept at around 2 bar for air, He and soap with the pressurised air provided by an external air compressor located outside the control room of the wind tunnel. A photograph of the seeding rake is given in Figure 20 of the Book of Reference of TWT2 [17]. Note that in certain cases the seeding rake was repositioned to ensure adequate seeding in the region of interest. This was done in cases without the passive grid (lower ambient turbulence intensity) since the initial position of the seeding rake could not ensure adequate seeding near the centre-plane of the canyon, even though it was perfectly positioned for the region towards the edge of the canyon. So, two different sets of measurements (i.e. two different fields of view) were obtained corresponding to the two different positions of the seeding rake.

2.2.3 Calibration of the Robotic PTV system

2.2.3.1 Geometric Calibration

The goal of the geometric calibration is to extract a mapping function that relates the particle image displacement in the image plane with the tracer particle displacement in the flow [6]. In the case of 3D PTV measurements, a standard calibration plate is used for geometric calibration. The calibration plate used for the experiment is the 395-54 SSSP (Figure 5). For the accomplishment of the calibration, the number of marks, their size, and their distances should be known. The 395-54 SSSP calibration plate has 42 markers with the distance between them being 54mm. The dimensions of the utilised calibration plate are 395mm \times 342mm (width \times height). Three open circles can be seen on the plane – the fiducials - and these should be discernible in all the calibration images of all employed cameras to determine the orientation of the calibration plate and the position of the coordinate system.

The following calibration procedure was implemented:

- I. Firstly, the calibration plate is placed at approximately the center of the measurement domain where also the $Y = 0$ (depth) position is defined.
- II. Different positions of the robotic arm (and by extension the mounted cameras) are programmed by using the RoboDK software. These positions result in different views of the same calibration plane. So, from one view to another, the relative position of each camera



with respect to the calibration plane changes. On the contrary, the relative position of the cameras with respect to each other stays the same.

- III. The captured calibration images are finally used to automatically extract the mapping function for each camera by using appropriate software (in our case the DaVis software). Inspection of the calibration images and manual selection of the fiducial points is usually also an option.

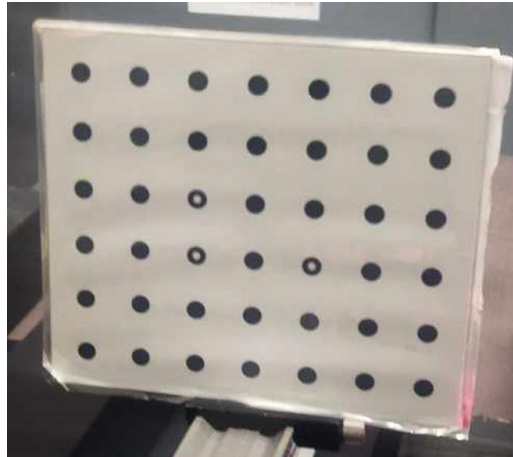


Figure 5. Calibration plate 395-54 SSSP used for geometric calibration.

2.2.3.2 Volumetric Self-Calibration

Volume self-calibration [18] accounts for remaining errors due to imperfect geometric calibration. As [18] denote, even if great care is taken during the geometric calibration, remaining errors in the range of 0.5–2 pixel can still be present. With 3D PTV, where triangulation of individual particles is implicated, these errors can be significant.

In order to perform volume self-calibration, actual particle image recordings are required (usually ~ 100 images are enough). By making use of the mapping function (of each camera), originating from the geometric calibration, as well as the aforementioned image recordings, the position of the particles in the real-world space is back-projected into the image space. The actual positions of the particles in the real-world space are known by matching and triangulation (see [18] for details). From the difference between the back-projected positions of the particles and the triangulated ones the disparity map is derived. For reasons of statistical representativeness, the average disparity within sub-volumes of the full measurement volume is computed. Note that the seeding should be less dense than that of actual 3D-PTV measurements. During the experiment, this was ensured by appropriately adjusting the pressures of the air, soap and helium from the control panel of the FSU. The described computational procedure is repeated until the disparity within each sub-volume is less than 0.1 voxel.

The calculation of the Optical Transfer Function (OTF) is feasible after volume self-calibration is performed. The OTF [19] accounts for inaccuracies in the shape of the captured particles due to astigmatism and/or defocusing and is particularly important when the working fluid is not air (i.e. in water channels).



2.2.4 Processing of PTV raw data

The generic workflow for the processing of PTV data is the following: (a) pre-processing, (b) Shake-the-Box, (c) post-processing, particle track stitching & binning. A more detailed description of each step is the following:

- a) Pre-processing: the aim of this step is the elimination of noise and therefore the enhancement of the intensity contrast between the particles and their background. This noise is principally caused by artificial or natural lighting during the experiment as well as reflections. This was done by subtracting the time-minimum intensity on a slide kernel of 5 or 7 images. For the latter pre-processing to be useful, the reflections should be stationary in time or at least they should have a relatively low dominant frequency in comparison with the acquisition frequency. This step was particularly important for the cases involving vegetation (hedges or roof greening) since the utilised foam material was prone to reflections and could not be painted with Musou Black [14] to avoid interfering with its aerodynamic behaviour.
- b) Processing: as already mentioned, the Shake-the-Box algorithm ([8], [9]) is used here instead of cross-correlation as done for PIV (see section 2.2.1). Shake-the-box is a particularly efficient and fast method based on image matching (minimisation of residuals between subsequent image recordings), yielding particle tracks (e.g. helium-filled soap bubbles following the flow). It is noted that a new track is added only if it consists of at least 4 particle trajectory positions corresponding to at least 4 consecutive time steps. Apart from appropriate seeding and accurate calibration (including geometric and volume self-calibration, see section 2.2.3), fine-tuning of certain parameters such as the allowed triangulation error and the minimum intensity threshold constitutes also an important aspect for a successful implementation of Shake-the-Box. Good practice is to initially use a subset (e.g. ~100 images) of the whole group of recordings which allows for trial-and-error definition of suitable values for the implicated parameters. This should be also done after each measurement acquisition to check if an adequate number of tracks is retrieved by the Shake-the-Box algorithm. Then, this setup can be used for processing the whole group of image recordings.
- c) Post-processing, particle track stitching & binning: it is possible that the final results contain “bad tracks” i.e. unphysical tracks that have to be removed. Usually, it is easy to detect them by visual inspection of the ensemble of tracks since they do not follow the adjacent particle trajectories. It is also frequent for these bad tracks to showcase unreasonable velocity (or acceleration) values, e.g. significantly higher than the free-stream velocity or a characteristic velocity of the problem. Furthermore, these tracks tend to be shorter than the correct ones. By taking advantage of these characteristics, a variety of post-processing tools can be applied to remove erroneous tracks. For example, one can apply a velocity and/or acceleration range filter limiting the allowed velocity/acceleration values in the ensemble of the extracted tracks. Another simple solution that can be applied in a complementary or exclusive fashion is the introduction of a higher minimum threshold for the allowed length of tracks than the default one which is equal to 4 in this case. Finally, more localised post-processing tools can be used, which take into account the velocities within a “neighborhood” of an examined track/velocity and the discrepancy of this from a statistical measure (e.g. the median) of these adjacent



velocities. Such tactics were applied to the processed data of this experimental campaign to reduce the number of bad tracks.

The next step is particle track stitching, where all tracks from individual acquisitions and views (pertaining to the same examined case e.g. at a specific Reynolds number) are combined, i.e., they are overlaid to form the complete measurement set within the examined volume. This was done in the current experimental campaign since each examined case consisted of multiple views (i.e. positions of the robotic arm and/or the seeding rake) and multiple acquisitions (see section 2.2.2.1).

Finally, the Lagrangian particle tracks should be somehow transferred/interpolated into an Eulerian frame. In this experimental campaign, where the focus is on the time-averaged velocity fields and their statistics, the implementation of binning [11] is the most convenient solution. With binning, the measurement volume is divided into bins of user-defined size and then ensemble-averaging is performed within each bin. Once particle track stitching between the different acquisitions is over, a high number of ensemble members (i.e. particles) should be expected within each bin. As a rule of thumb, the minimum number of ensemble members within each bin should be at least 50-100. The size of the bin (and therefore the spatial resolution) is implicitly limited by this minimum number of ensemble members.

2.3 Complementary measurements

The extracted PTV dataset was complemented with surface pressure and hot-wire measurements using the equipment of NTUA. More details for both the complementary measurements are given in the following subsections.

2.3.1 Surface pressure measurements

Pressure taps were installed on the fourth model building (upstream building of the examined canyon). 18 pressure taps (6 per side) are located at the centre-line of this building as can be seen in Figure 6. The exact position of the pressure taps will be given in the figures illustrating the results (see Section 4).

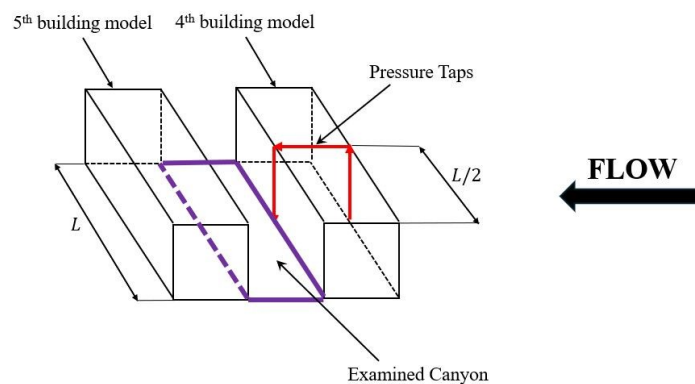


Figure 6. Schematic illustration of the position of the pressure taps relative to the examined canyon and the approaching flow.

The same building model was used in both facilities (the model was shipped between Athens and Delft) to obtain surface pressure measurements. In this way, any uncertainty originating from the model itself was eliminated. A pressure measurement system consisting of tubes mounted on the pressure taps and directly connected to a 24-channel pressure scanner (PSC24 made by SVMtec) was employed. This pressure scanner enabled the acquisition of synchronous measurements for all pressure taps. The total and static pressures were also measured at the same time, at two different positions: (a) above the examined canyon's floor, in the undisturbed flow region, (b) slightly upstream of the 1st building model and near the ceiling of the wind tunnel. A Pitot-static tube was used in both cases. The difference in the dynamic pressure between the two positions was consistently less than 9%. The sampling frequency was 50Hz (maximum sampling frequency of PSC24) and the acquisition time was equal to 90 seconds.

2.3.2 Hot-wire measurements

Hot-wire anemometry is employed for the acquisition of high-frequency velocity measurements. An IFA 300 measurement system with a single hot-film Model 1201 TSI probe was used. The probe was mounted onto an electrically powered and electronically controlled 3D traversing system to locate it at the desired positions. The sampling frequency was set to 1kHz while the acquisition time was 64 seconds. The calibration of the measurement system was performed in-situ prior to the measurements. This calibration was repeated once per day until the end of the measurements. A polynomial of 4th order was used as the calibration function with the fitting error being consistently below 2%.

The acquired measurements fall into two different categories: (a) characterisation of the developed boundary layer on the roofs of the 3rd, 4th and 5th building models (comprising the examined canyon) and (b) quantification of the approaching flow in front of the whole model. The measurements were obtained for both the cases with and without the passive grid (i.e. with higher and lower ambient turbulence intensity). The exact positions of the acquired velocity profiles can be seen in [Figure 7](#) for both the (a) and (b) categories. In particular, the velocity profiles were measured along the red lines shown in [Figure 7a](#) and [Figure 7b](#). For convenience, all planes at the same height are outlined in the same colour in each figure.

It can be seen from [Figure 7a](#) that the measurements were conducted exactly at the center of the roofs of the 3rd (L_3), 4th (L_1) and 5th (L_2) model buildings. From [Figure 7b](#), it is seen that the velocity was measured on the centre-line ($Y = 0$) and near one end of the canyon ($Y = L/2$). The starting height of both velocity profiles of [Figure 7b](#) is $Z = 0.93H$.



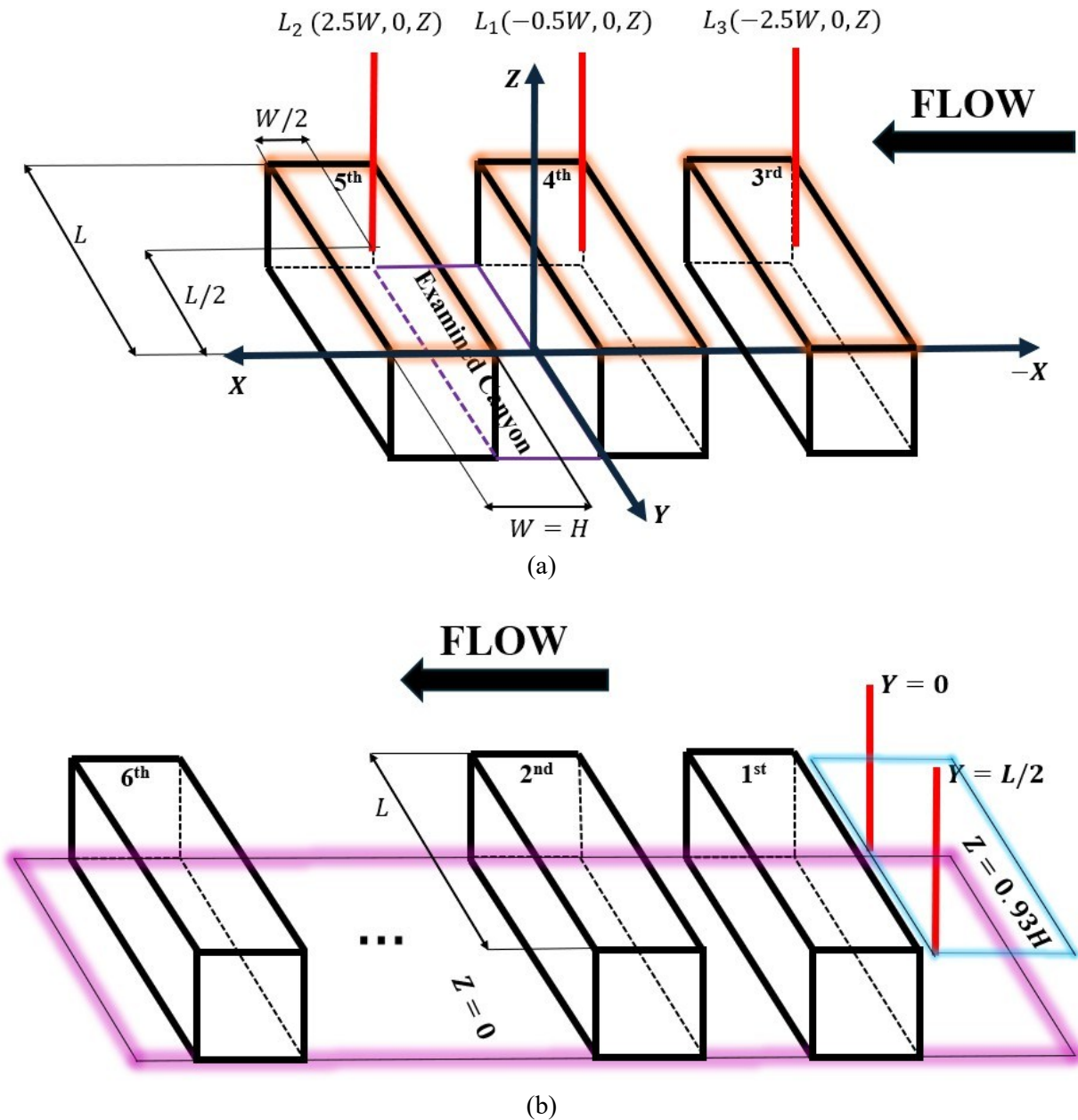


Figure 7. position of measured velocity profiles (red lines) for: (a) characterisation of the developed boundary layer on the roofs of the 3rd, 4th and 5th building models. The geometric loci of the lines are also given in parentheses. (b) quantification of the approaching flow in front of the whole model. The same coordinate system applies to both figures.

2.4 Safety Instructions

Since LEDs were utilised instead of high-energy lasers, there are no significant safety concerns. However, staring directly at the LED while it operates should be avoided. General safety instructions are given in the Book of Reference of TWT1 [20]. Other safety instructions, specific to this experiment, are the following:

- When helium-filled soap bubbles are used as seeding, the wind tunnel floor becomes very slippery. Therefore, if for some reason the scientific staff has to enter the wind tunnel section between runs, great care should be taken. The existence of the robotic arm, the LEDs and the model itself (Figure 3) make such a task considerably more difficult. It is imperative to wash the soap off the section's floor once the experimental campaign is complete.
- Extreme caution is required during the operation of the air compression system. All limits referring to temperature or pressure (e.g. temperature of the motor, oil pressure etc.) must be monitored and always respected.¹

2.5 Model Preparation

A key component of every wind tunnel test is the preparation of a suitable model corresponding to the needs of the experiment that is to be conducted. In the current framework, this includes:

- Suitable choice of the model material for minimal roughness, optical access (glass or plexiglass), durability (scratches) etc. For the present PTV applications, the utilised material should minimise reflections, otherwise the captured images will be contaminated by noise. If, for any other reason, the chosen material is such that reflections cannot be completely avoided, other measures should be taken e.g. using non-reflecting paint such as the Musou Black. As already mentioned, Musou Black paint had been used on multiple occasions during the experiment. It is reminded that due to the presence of HFSB seeding the coat of paint may come off and should be renewed as frequently as possible. The construction of the models was outsourced to external partners who built them from PVC. The model was mounted onto a splitter plate made of MDF. The leading edge of the splitter plate was shaped to form an angle of approximately 30° – 45°. This was done to reduce or eliminate the stagnation region. The splitter plate was initially placed more than 30 cm away from the ground to avoid boundary layer (BL) effects since inherently (without making use of roughness elements) a BL of about 20-30 cm is developed inside the test section. The splitter plate (with the models on) had to be lifted even more since its initial position was not compatible with the position of the seeding rake (i.e. the seeding was not enough inside the examined canyon). Appropriate ribs were used to elevate the splitter plate from the ground. The building models were mounted onto the splitter plate by using double-sided tape. A schematic illustration (top view) of the whole model is given in Figure 8.

¹ Disclaimer: these are safety measures specific to the NTUA lab and the current experiment. Although similarities with the measures necessary for other labs may occur, they are by no means exhaustive or sufficient and additional/alternative safety measures may be required in other labs.

If surface pressure measurements are also required, additional care should be taken to ensure that appropriate pressure taps are mounted onto the surfaces of interest. The position of the pressure taps was given in section 2.3.1. The taps were drilled down by the scientific staff of the lab and tubes were flushed with the external surfaces of the 4th building model (Figure 6). A hole was created (Figure 8) on the splitter plate to lead the tubes outside the test section.

- For the simulation of vegetation, porous material (foam) with PPI20 (i.e. 20 pores per inch) was used for both the hedges and the roof greening. The model of the hedges had height and width of 10 mm (6.66% of the height/width of the street canyon) while its length was equal to the length of the canyon L . The hedges were positioned equidistantly from the walls of the buildings comprising the examined canyon, spanning its whole length (parallel to the buildings). The roof greening covered the roofs of both building models of the examined canyon while its height was equal to 5 mm (3.33% of the height/width of the canyon). Note that for buildings of 30 m height (scale factor equal to 1:200), the full-scale dimensions of the hedges and the roof greening are 2 m and 1 m, respectively. The same foam material as in [21] was used with pressure loss coefficient at reduced-scale equal to about $\sim 500 \text{ m}^{-1}$ for both types of vegetation. More details regarding modelling of vegetation are given in [21]. All the aforementioned details for the vegetation are depicted in Figure 9.
- It should be ensured that a low value of blockage ratio (usually less than 5%) is maintained when the model is installed inside a closed-loop wind tunnel. This value is less than 4% in our case. However, the existence of the LEDs and the robotic arm inside the section is not taken into account for this calculation.

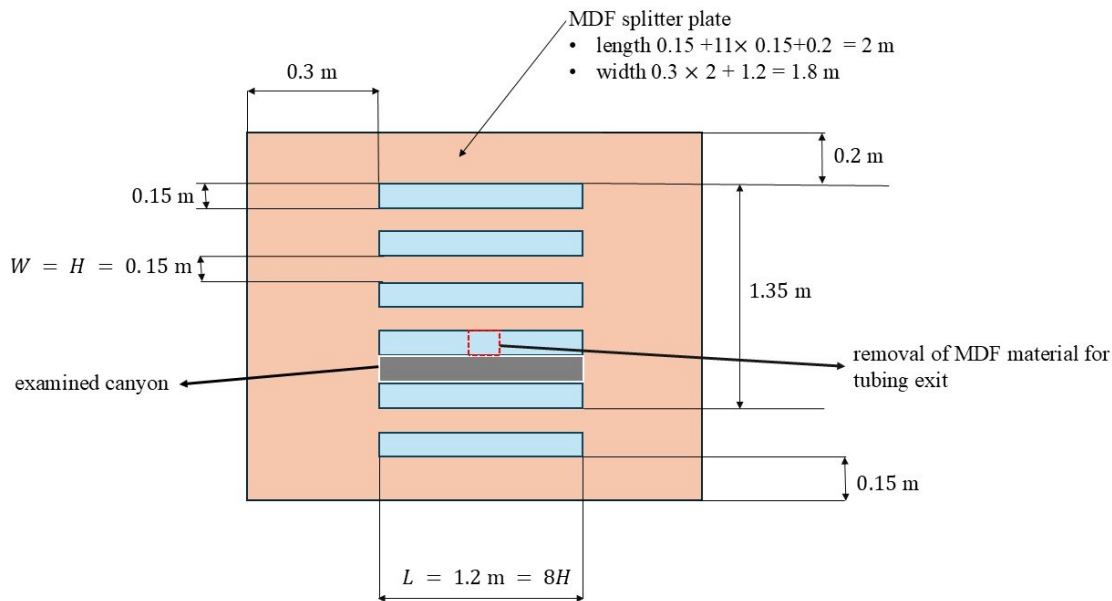


Figure 8. Geometric configuration of the building models and structural details.

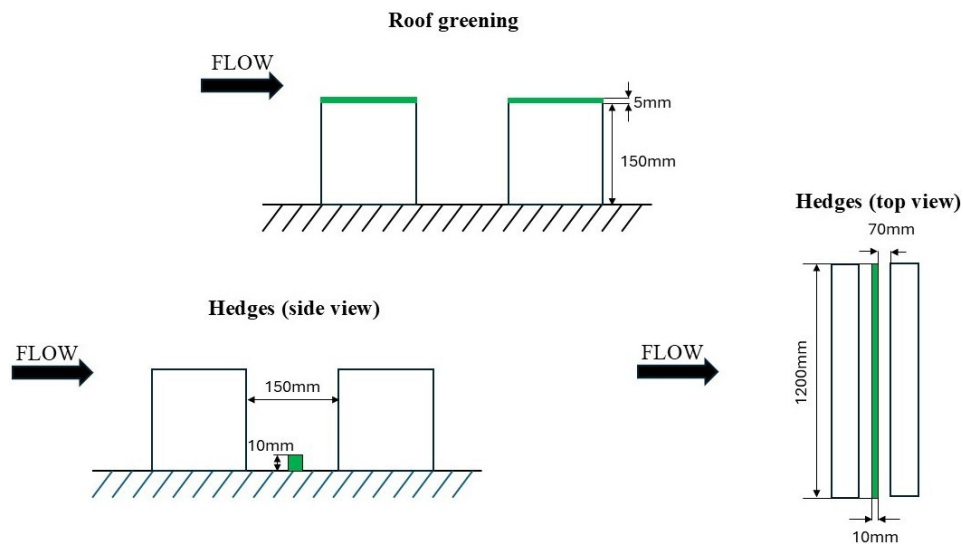


Figure 9. Schematic illustration of the position of vegetation with respect to the examined canyon along with the necessary dimensions.

2.6 Reference velocity and background flow

The reference velocity was determined by measuring at the same time the dynamic pressure and the temperature. The temperature is utilised to calculate the density through an equation of state incorporating information for the barometric pressure and the relative humidity of the air. The latter atmospheric data are obtained by a meteorological station located at the roof of the building which houses the wind tunnel facility. With known density and dynamic pressure, the velocity can be computed. The dynamic pressure is measured by a Pitot tube located slightly upstream of the whole model (Figure 8) and near the ceiling of the wind tunnel. A Pt100 thermometer (range 0-50°C, accuracy 0.0236°C) located inside the test section is used for measuring the temperature. For the dynamic pressure, an FCO432 differential pressure transmitter (Furness Controls Ltd) with range ± 150 Pa was used. Finally, the Reynolds number $Re = U_\infty H / \nu$ can be computed with $U_\infty, H = 0.15$ m and $\nu = 1.5 \cdot 10^{-6}$ m²/s being the free-stream velocity, the height of the building models and the kinematic viscosity at 20°C, respectively.

The approaching flow was quantified in front of the whole model (upstream of the 1st building) by means of hot-wire anemometry, as already shown in Figure 7b. Two velocity profiles were measured at: (1) $Y = L/2$ (near the one lateral end of the model) and (2) $Y = 0$ (centre-line) in front of the 1st building. Note that the spanwise extent of the measurement volume within the examined canyon ranges from $Y = L/2$ to $Y = 0$. This was mainly done to gain some insight into the approaching flow. The velocity profiles were extracted with and without the presence of the passive grid, for the minimum and maximum tested Reynolds numbers i.e. $Re = 25000$ and $Re = 60000$. The time-average velocity as well as the turbulence intensity for both Reynolds numbers are given in Figure 10 and Figure 11, for the cases without and with the passive grid, respectively.

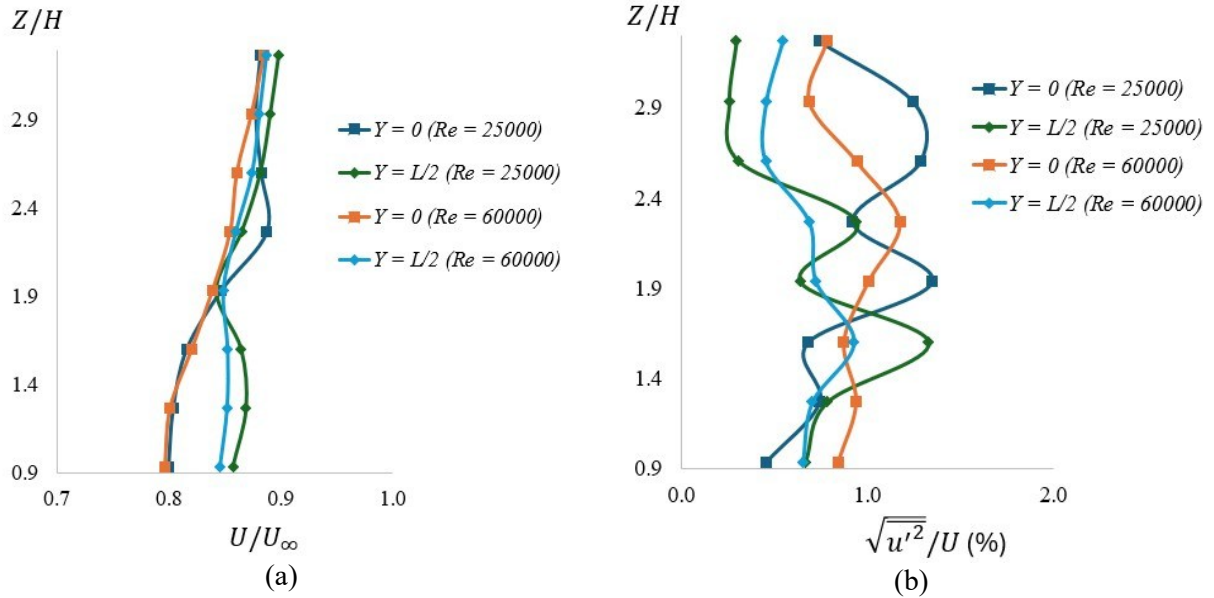


Figure 10. Profiles of the approaching flow at two different positions (see Figure 7b) i.e. $Y = 0$ and $Y = L/2$ for: (a) the time-average, non-dimensional velocity U/U_∞ and (b) the turbulence intensity $\sqrt{u'^2}/U$ where u' is the streamwise velocity fluctuation. The results pertain to the case without the passive grid (low ambient turbulence intensity).

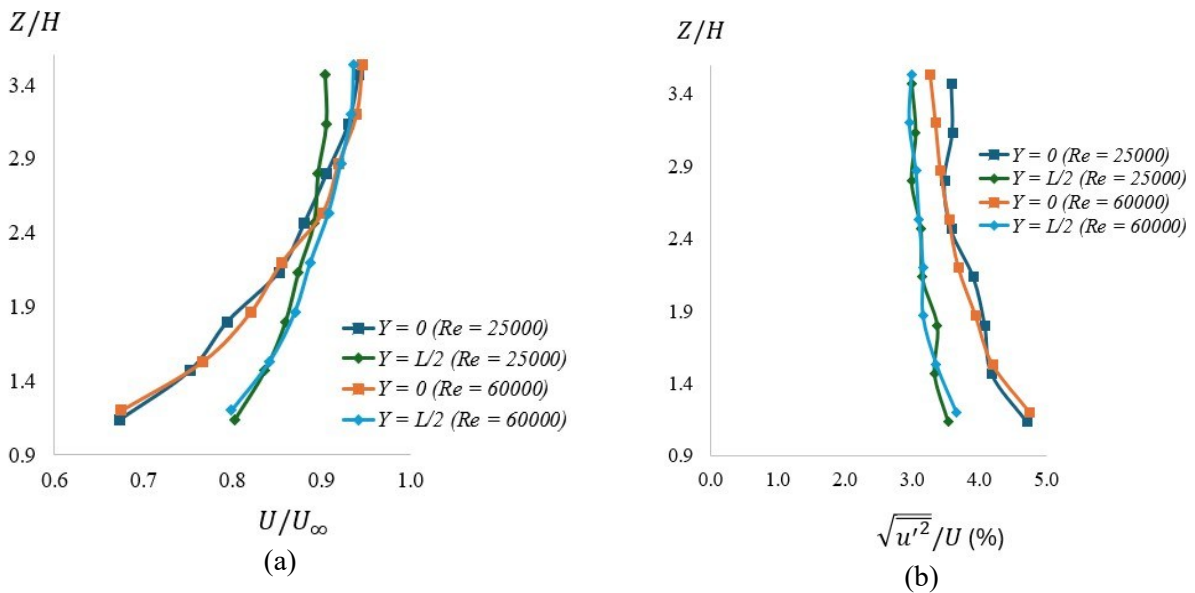


Figure 11. Profiles of the approaching flow at two different positions (see Figure 7b) i.e. $Y = 0$ and $Y = L/2$ for: (a) the time-average, non-dimensional velocity U/U_∞ and (b) the turbulence intensity $\sqrt{u'^2}/U$ where u' is the streamwise velocity fluctuation. The results pertain to the case with the passive grid of Figure 1c (higher ambient turbulence intensity).

The main conclusions/observations derived from Figure 10 and Figure 11 are the following: (i) the presence of the passive grid increases the turbulence intensity by 4-5%, (ii) Reynolds number independence holds for both cases, i.e. with and without the passive grid. In particular, the absolute differences between the two different Reynolds numbers are below 0.04 (in U/U_∞ units) for the velocity and below 0.6% for the turbulence intensity, (iii) the difference between the profiles at different locations for the case without the passive grid is not as pronounced as for the case with the passive grid. More specifically, the absolute differences between the central ($Y = 0$) and the lateral ($Y = L/2$) velocity profiles are below 0.065 (in U/U_∞ units) for the case without the passive grid while when the passive grid is used the maximum value is 0.13. The respective differences for the turbulence intensity are 0.99% and 1.2%. Note that the previous values are the maximum absolute differences for both Reynolds numbers. It should be noted though that these measurements are influenced by the presence of the model, and they do not strictly represent asymmetries found in the (empty) wind tunnel facility.

Another investigation pertains to the development of the boundary layer on the roofs of the building models. A comparison between the (time-average velocity and turbulence intensity) profiles along the lines L_1 , L_2 and L_3 (see Figure 7a) is presented here in Figure 12, at a Reynolds number equal to 60000 and for the case with the passive grid applied on the inlet of the test section. For the case without the passive grid and at the same Reynolds number, a similar comparison is given in Figure 13 along the lines L_1 and L_2 (4th and 5th buildings, see Figure 7a).

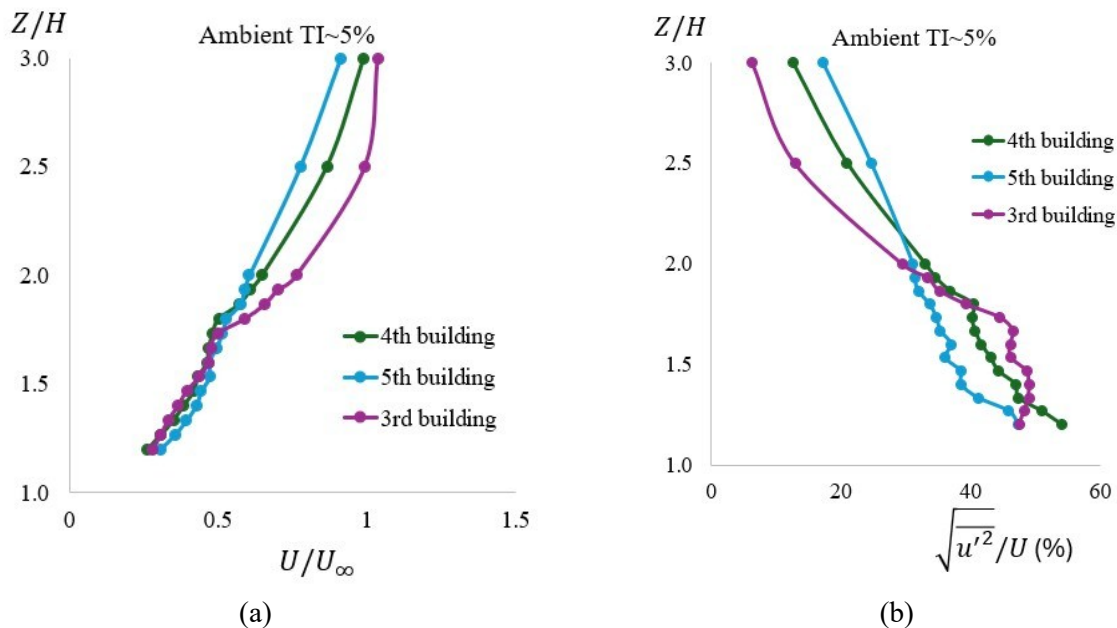


Figure 12. A comparison between the profiles along the lines L_1 ($X = -0.5W, Y = 0, Z$), L_2 ($X = 2.5W, Y = 0, Z$) and L_3 ($X = -2.5W, Y = 0, Z$) (see Figure 7a) corresponding to the center of the roofs of the 4th (green), 5th (blue) and 3rd (purple) building models, respectively. This comparison is made for: (a) the time-average, non-dimensional velocity and (b) the turbulence intensity. The Reynolds number is equal to 60000 and the passive grid of Figure 1c had been applied on the inlet of the test section (ambient turbulence intensity $\sim 5\%$).

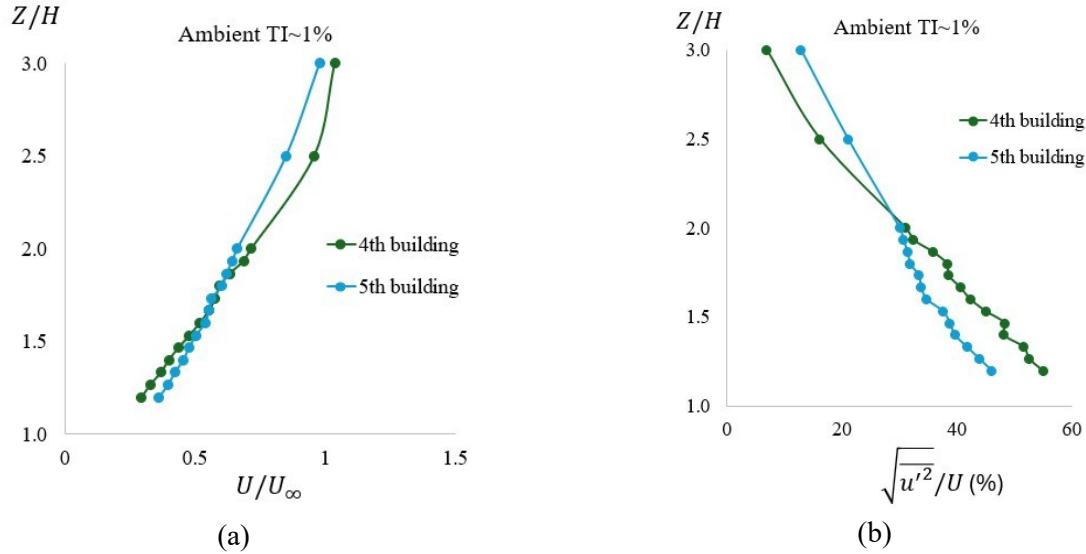


Figure 13. A comparison between the profiles along the lines $L_1(X = -0.5W, Y = 0, Z)$ and $L_2(X = 2.5W, Y = 0, Z)$ (see Figure 7a) corresponding to the center of the roofs of the 4th (green) and 5th (blue) buildings, respectively. This comparison is made for: (a) the time-average, non-dimensional velocity and (b) the turbulence intensity. The passive grid was not applied on the inlet of the test section (ambient turbulence intensity $\sim 1\%$), and the Reynolds number is 60000.

For both cases (with and without the passive grid), the velocities on the roofs of the buildings are in good accordance with each other until about $Z/H = 2$. This cannot be said for the turbulence intensity though since there is consistently a non-negligible discrepancy between the profiles at different locations. It is interesting to note though that there is a point of intersection for the different turbulence intensity profiles at $Z/H = 2$, for both experimental setups (i.e. with and without the grid). [22] found that the flow inside the 3rd, 4th, 5th and 6th street canyons (out of 7) demonstrated similar flow behaviour. However, they did not focus on the roofs of the buildings. Thus, the current investigation may add new information to the existing literature implicating similar configurations i.e. subsequent street canyons.

3 TU Delft - Equipment and methods. Training and Documentation.

3.1 Introduction

3.1.1 The TU Delft Open Jet Facility (OJF)

The open jet facility is under the TU Delft Faculty of Aerospace Engineering. It is situated in a large room with a width of 13 meters and a height of 8 meters. The flow in the OJF is driven by a large fan powered by a 500kW electric engine. The velocity can be safely and reliably adjusted in the range 3 m/s – 35 m/s. After the large fan, the flow passes through a long diffuser, and it is guided by two rows of corner vanes in order to be rotated by 180 degrees. The flow enters a second diffuser, in which a wire mesh inhibits flow separation. In the settling chamber, the flow passes through several screens that reduce velocity deviations and turbulence in the flow (attainable turbulence intensity lower than 1%). Then, through a contraction a smooth flow is obtained into the open test section. The size of the OJF outlet is 2.85x2.85. At the end of the test section, the flow is cooled by a 350kW radiator system to compensate for the added heat in the flow. Finally, before entering the fan, the flow is redirected 180 degrees again by two rows of corner vanes. It is worth mentioning that there is a large staging room adjacent to the test section where preparatory tasks (e.g. assembly of the models, testing of the equipment etc.) can be realised in parallel with ongoing experiments. A schematic illustration of the facility is given in [Figure 14a](#) (adjusted from [\[23\]](#)). In [Figure 14b](#), a photograph of the outlet of the OJF is given.

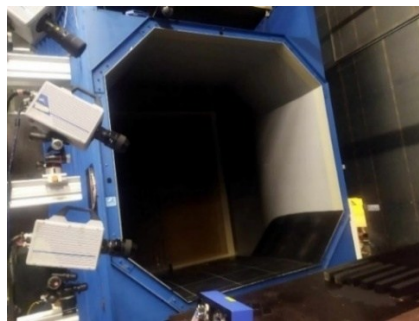
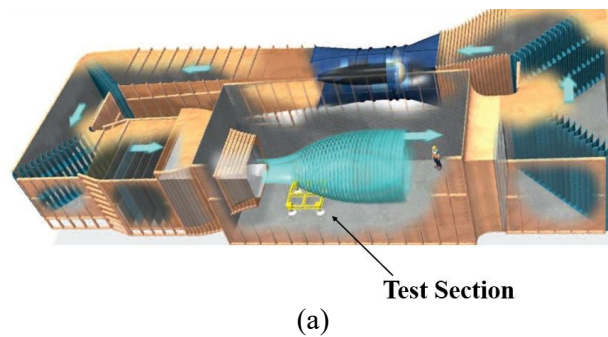


Figure 14. (a) schematic illustration of the open jet facility (adjusted from [\[23\]](#)) and (b) a photograph of the outlet of the open jet facility. The cameras as well as the small street canyon models can be also seen.

3.2 PTV measurements

3.2.1 Components of the PTV system

3.2.1.1 Cameras

Three high-speed Photron Fastcam SA1.1 cameras were used for the experiment with a sensor resolution of 1024x1024 and a pixel size of 20x20 μ m. The maximum acquisition frequency of the cameras is 5400 Hz at full resolution. The cameras were mounted vertically on appropriate beams as illustrated in [Figure 15a](#), to ensure optical access inside the canyon of interest. The position of the cameras relative to the examined street canyon can be retrieved by observing [Figure 1b](#) (Camera 2 and 3 are shown).

When the large building models were used ([Figure 1b](#)), two different fields of view, namely FoV1 and FoV2, were necessary to cover the whole measurement volume i.e. half of the examined street canyon. The other half was not measured due to symmetry. FoV1 and FoV2 corresponded to two measurement volumes: one volume towards the canyon's lateral end and another one incorporating the region near the centre-plane, respectively. The whole structure, shown in [Figure 15a](#), was moved accordingly to cover the second field of view while slight movement (yaw, pitch and tilt around the corresponding axes) of the cameras was also necessary. Care was taken to ensure that there was an overlap between the two different measurement volumes (i.e. by making use of appropriate markers on the roofs of the buildings). For the small buildings, only one field of view was sufficient to cover half of the examined canyon. Several objects can be used as markers to help in finding the correct positions of the cameras. This can be seen in [Figure 15b](#), where a measuring tape was utilised as a reference to ensure that the field of view encompassed the correct measurement volume (half of the 4th canyon) for the configuration with the small building models.



Figure 15. (a) configuration of the cameras and (b) utilisation of a measuring tape as a reference during focusing of the cameras (small building models, [3]).

For all configurations Nikkor lenses were used with their focal lengths f listed in [Table 1](#). In [Table 2](#) the values of $f\#$ (defining the aperture which is the same for all cameras per configuration),

the magnification factor M and the digital image resolution are given. The reader is referred to [6] for more information regarding the predetermination/calculation of these parameters.

| Case | Camera 1 | Camera 2 | Camera 3 |
|--|----------|----------|----------|
| large models: FoV1 + FoV2 | 50 mm | 35 mm | 35 mm |
| small models: the whole half of the canyon | 180 mm | 105 mm | 105 mm |

Table 1. Focal length f (mm) of the employed lenses for all cameras in both scenarios (large and small models).

| Case | $f\#$ | M | pixel/mm |
|---|-------|------|----------|
| large models: FoV1 (towards the lateral edge of the canyon) | 16 | 0.04 | 1.98 |
| large models: FoV2 (towards the centre of the canyon) | 16 | 0.03 | 1.52 |
| small models: the whole half of the canyon | 22 | 0.08 | 4 |

Table 2. $f\#$, magnification factor M and digital image resolution (pixel/mm) for all field of views in both scenarios (large and small models).

The value of the acquisition frequency was chosen depending on the different Reynolds numbers as already explained in section 2.2.2.1. The parameter $a \in \mathbb{N}$ (Equation (3)) was 5 for all the acquisitions (different Reynolds numbers and cases with vegetation) whenever the large models were used while it ranged from 1 to 3 for the case of the smaller models. The number of acquired vortex turnovers was kept higher than 95 for all cases. However, for a couple of cases, a was finally reduced to 4 due to processing issues and as a result the number of processed vortex turnovers was also reduced to 76.

3.2.1.2 Illumination

The same LEDs (LaVision LED Flashlight 300s) were used as those in Athens (section 2.2.2.2). Two LEDs were necessary to ensure adequate illumination inside the canyon for FoV2 and the case with smaller models while for FoV1 only one LED was sufficient. By using 2 LEDs for FoV2, adequate intensity contrast between the particles and the background was obtained and enough particles (and particle tracks) could be identified. Additionally, the use of a specific lens was also examined, to transform the LED light (non-collimated) to more collimated light (“laser-type” light) but finally it was not deemed necessary.

Musou Black paint was used, as done in Athens, to minimise the background light reflections within the field of view of the cameras.

3.2.1.3 High-speed Controller

The Programmable Timing Unit (PTU) X was used to synchronise the illumination from the LED and the acquisition by the cameras, see Figure 16. The PTU X is connected to the computer which is basically responsible (through appropriate software e.g. DaVis) for the synchronisation of the latter components.





Figure 16. The utilised Programmable Timing Unit (PTU-X) responsible for the synchronisation of cameras and the LED lights.

3.2.1.4 Seeding

Similarly with the experiment at NTUA (see section 2.2.2.3), a seeding rake was responsible for the generation of neutrally buoyant helium-filled soap bubbles. The seeding rake was located inside the contraction of the OJF and was larger than the one used in the wind tunnel of NTUA. The dimensions of the OJF seeding rake are 1m x 2m while it consists of 400 nozzles and 8 rakes. Slight readjustment of the position of the rake was again necessary to ensure that for every different field of view (Table 1 and Table 2) sufficient seeding was present. The seeding rake was again controlled by an FSU. The control panel of the FSU can be seen in Figure 17.



Figure 17. Control panel of the Fluid Supply Unit (FSU).

3.2.2 Calibration of PTV system

The calibration of the PTV system consists of three individual steps: the intensity calibration, the geometric calibration and the volume self-calibration. A detailed description of these steps is given in the following subsections.

3.2.2.1 Intensity Calibration

The intensity calibration aims at the removal (subtraction) of the inherent background noise due to the operation of the cameras. The most usual way to do it is to put the caps of the lenses on (lenses are shuttered) and then perform the intensity calibration. In cases where the experimental setup is too delicate and geometric calibration has already been done, putting the caps on for every intensity calibration is not ideal because even the slightest movement could necessitate new geometric calibration. An alternative solution is to put an object which is painted black (or preferably Musou Black) in front of each lens (one after the other) and then perform the intensity calibration separately for each camera. With the previous solution, the possibility of moving the cameras is significantly reduced. This was done during the experiments in the OJF. A good practice is to repeat the intensity calibration for every new acquisition frequency.

3.2.2.2 Geometric Calibration

For the geometric calibration, the same calibration plate used in the NTUA experiment was employed (Figure 5). The following calibration procedure was applied during the experiment, which is similar to the one presented in the Book of Reference of the TWT2 [17]:

- I. Firstly, the calibration plate is placed at approximately the center of the measurement domain where also the $Y = 0$ (depth) position is defined.
- II. The position of the calibration plate is moved in the depth direction (Y –axis) to approximately span the whole measurement volume while it is rotated at the same time. Simultaneous rotation and translation are permitted by the utilised DaVis software, simplifying the calibration procedure. Otherwise, the classic procedure consisting of parallel translation of the calibration target along the Y -axis should be followed. It is evident that this classic procedure is more tedious since perfect alignment with the Y -axis should be ensured for each different position of the calibration target. The main difference from the calibration of the Robotic PTV system presented in section 2.2.3.1 is that the position of the calibration target changes relative to the cameras instead of moving the cameras. Both calibration procedures are equivalent, as they rely on the relative position change between the cameras and the calibration target.
- III. The captured calibration images are finally used to automatically extract the mapping function for each camera by using appropriate software (in our case the DaVis software). Inspection of the calibration images and manual selection of the fiducial points is usually also an option.

The following are some tips and comments for efficient calibration:

- New calibration is required not only for every different field view but also in case that the experimental setup (i.e. system of cameras) is accidentally (and sometimes even minutely) disturbed with respect to its previous position. This was the case in this experiment where the experimental setup was very sensitive to movements. For this reason, the direct exposure of



the cameras to the approaching flow should be avoided. However, a new volume self-calibration can be sufficient without having to geometrically calibrate again.

- Enhancement of the lighting during the calibration may be necessary to ensure that the markers of the calibration plate are discernible by all the employed cameras and for all the positions of the calibration plate.
- Generally, extrapolation of the mapping function should be avoided at least for important parts of the measurement volume (e.g. inside the canyon). This means that the different positions of the calibration plane should cover as much as possible the measurement volume.

3.2.2.3 Volume Self-Calibration

Volume Self-Calibration accounts for remaining errors due to imperfect geometric calibration by making use of actual particle image recordings. More details are given in section 2.2.3.2 and in [18].

3.2.3 Processing of PTV raw data

The generic workflow for processing the PTV data is the following: (a) pre-processing, (b) Shake-the-Box, (c) post-processing, particle track stitching & binning. A more detailed description of each step has already been given in section 2.2.4.

3.3 Surface Pressure Measurements

The position of the pressure taps on the (4th building model) is exactly the same as the one presented in section 2.3.1. For the pressure measurements a DSA3217/3218 Series Scanivalve Pressure Scanner (600 Pa pressure module, accuracy 0.1%) was used. The sampling frequency was set to 1kHz, and the acquisition time was 60 seconds.

3.4 Safety Instructions

General safety measures are given in the Book of Reference of TWT1 [20] while case-specific safety instructions are similar to those given in section 2.4.

3.5 Model Preparation

The preparation of the model was similar to that already presented in section 2.5. It is noted that the geometric configuration was the same as the one shown in Figure 8. The same applies also to the cases with vegetation (Figure 9). The construction of the models was partially outsourced to external partners who were responsible for manufacturing wooden plates intended to serve as the buildings' walls. The final assembly was completed by the scientific staff working on this experiment.



3.6 Reference Velocity

The reference velocity was automatically adjusted through a control system which uses as feedback the signal from a Pitot tube located at the settling chamber of the OJF (see section 3.1.1) and changes the rotational speed of the fan accordingly. The accuracy of this automatic adjustment was in the range 0.01-0.1 m/s. The control panel through which the WT user can define the reference velocity is shown in the following figure:



Figure 18. Control panel for the automatic adjustment of the reference velocity.

4 Results

4.1 Test matrices

Before proceeding to the presentation of the results, the test matrices of the experiments undertaken at TU Delft and NTUA are given in [Table 3](#) and [Table 4](#), respectively. Some comments regarding the test matrices are the following:

- The last column of both tables denotes whether a specific experiment has also been performed in the other wind tunnel facility. In this way, it is easy to determine the overlap between the two experimental campaigns.
- The *low turb* or *high turb* characterization in [Table 4](#) refers to the cases without and with the passive grid ([Figure 1c](#)) leading to lower ($\sim 1\%$) or higher ($\sim 5\%$) ambient turbulence intensity, respectively. This categorisation is pertinent only to the experimental campaign that took place at NTUA, as already mentioned.
- These test matrices present the cases for which PTV measurements were conducted.

| Configuration | Re | Volume | NTUA data |
|----------------|---------|---------------------|----------------|
| smaller canyon | 10,000 | half of the canyon | no |
| smaller canyon | 13,333 | half of the canyon | no |
| smaller canyon | 16,667 | half of the canyon | no |
| smaller canyon | 23,333 | half of the canyon | yes (at 25000) |
| smaller canyon | 26,667 | half of the canyon | no |
| smaller canyon | 30,000 | half of the canyon | yes |
| smaller canyon | 40,000 | half of the canyon | yes |
| Bare canyon | 30,000 | half of the canyon | yes |
| Bare canyon | 40,000 | half of the canyon | yes |
| Bare canyon | 50,000 | half of the canyon | yes |
| Bare canyon | 60,000 | half of the canyon | yes |
| Bare canyon | 80,000 | half of the canyon | no |
| Bare canyon | 100,000 | half of the canyon | no |
| Hedge | 40,000 | around centre-plane | no |
| Hedge | 60,000 | half of the canyon | yes |
| Hedge | 80,000 | around centre-plane | no |
| Roof greening | 40,000 | around centre-plane | no |
| Roof greening | 60,000 | half of the canyon | yes |
| Roof greening | 80,000 | around centre-plane | no |

Table 3. Test matrix containing the individual experiments conducted in the open jet facility of TU Delft. The smaller canyon had an $h = 0.05$ m and the larger canyon, where greening was also tested, had $h = 0.15$ m.



| Configuration | Re | Volume | TU Delft data |
|---------------------------|--------|--------------------|---------------|
| Bare canyon (low turb) | 25,000 | half of the canyon | no |
| Bare canyon (low turb) | 30,000 | half of the canyon | yes |
| Bare canyon (low turb) | 40,000 | half of the canyon | yes |
| Bare canyon (low turb) | 50,000 | half of the canyon | yes |
| Bare canyon (low turb) | 60,000 | half of the canyon | yes |
| Hedge (low turb) | 60,000 | half of the canyon | yes |
| Roof greening (low turb) | 60,000 | half of the canyon | yes |
| Bare canyon (high turb) | 25,000 | half of the canyon | no |
| Bare canyon (high turb) | 30,000 | half of the canyon | no |
| Bare canyon (high turb) | 40,000 | half of the canyon | no |
| Bare canyon (high turb) | 50,000 | half of the canyon | no |
| Bare canyon (high turb) | 60,000 | half of the canyon | no |
| Hedge (high turb) | 60,000 | half of the canyon | no |
| Roof greening (high turb) | 60,000 | half of the canyon | no |

Table 4. Test matrix containing the individual experiments conducted in the wind tunnel facility of NTUA.

4.2 PTV Uncertainty

In this section, a quick discussion of PTV uncertainty is made. It is imperative to have knowledge of the uncertainty in order to correctly interpret the differences between different configurations and/or Reynolds numbers. DaVis software is capable of calculating measurement uncertainties with respect to each direction, i.e. ε_U , ε_V , ε_W , in m/s. The uncertainty magnitude $\varepsilon = \sqrt{\varepsilon_U + \varepsilon_V + \varepsilon_W}$ is used here as the basis of the discussion. More specifically, the following global metric is used to quantify the uncertainty of the individual experiments: $\varepsilon_{97.5\%}/U_{ref}$. The $\varepsilon_{97.5\%}$ metric, calculated using DaVis software, defines an uncertainty range $[0, \varepsilon_{97.5\%}]$ within which 97.5% of the entire measurement set (i.e. ensemble of tracks) falls. This is done by means of a histogram extracted by DaVis. This metric is calculated for every acquisition of the same experiment e.g. a specific Reynolds number. Thus, a more detailed examination of the quality of the processing is ensured. Finally, the acquisition-averaged value is derived i.e. $\langle \varepsilon_{97.5\%} \rangle / U_{ref}$ (%) and shown for the *low turb* and *high turb* configurations at NTUA and the basic configuration at TU Delft and for every available *Re* number, in [Figure 19](#).

It is observed that the uncertainty is lower than 5% for all cases except the *low turb* one at $Re = 25000$. Note that $\langle \varepsilon_{97.5\%} \rangle / U_{ref}$ (%) is a conservative metric, since generally the flow demonstrates lower uncertainty values ($\sim 2\text{-}3\%$) than the $\varepsilon_{97.5\%}$ threshold within the canyon. An indication of this behaviour is shown in [Figure 20](#) where standard uncertainty magnitude (see [\[24\]](#)) profiles are given for the *low turb* and *high turb* NTUA configurations as well as the basic TU Delft one at $X/H = 0.5$

and $Y/H = 0$ i.e. the centre-line of the plane of symmetry (see Figure 7) at $Re = 60000$. For the latter calculation, the standard uncertainty is firstly computed for each velocity component [24] and then the standard uncertainty magnitude is derived and presented in Figure 20. Note that the uncertainty profiles of Figure 20 are derived after binning of the processed results unlike the values of the global metric shown in Figure 19. For more information regarding uncertainty quantification the reader is referred to [25], [26] and [27].

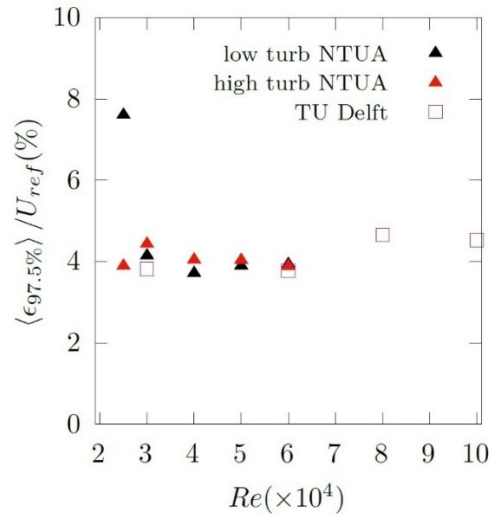


Figure 19. Global uncertainty metric $\langle \epsilon_{97.5\%} \rangle / U_{ref}$ (%) for the *low turb* and *high turb* configurations at NTUA and the basic configuration at TU Delft. The value of the latter metric is given for every available Re number.

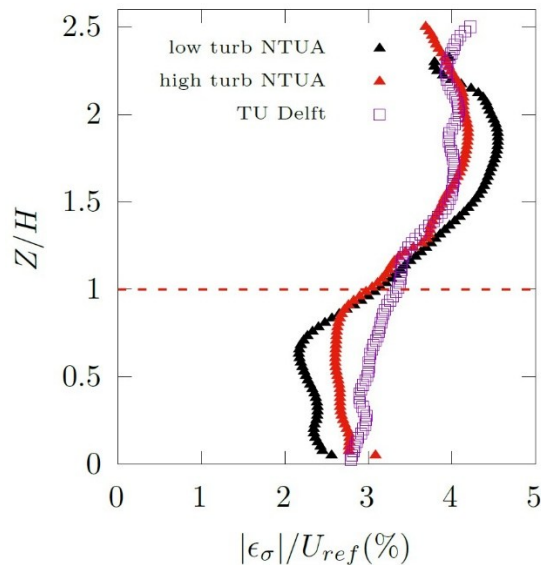


Figure 20. Standard uncertainty magnitude profiles for the *low turb* and *high turb* NTUA configurations as well as the basic TU Delft one at $X/H = 0.5$ and $Y/H = 0$ i.e. the centre-line of the plane of symmetry, at $Re = 60000$.

4.3 Scaling effects

4.3.1 Hot-wire measurements

As explained in section 2.3.2 hot-wire measurements were performed in the wind tunnel of NTUA along the two red lines of Figure 7a i.e. above the center of the buildings' roofs comprising the examined (4th) street canyon. The profiles along the $L_1(X = -0.5W, Y = 0, Z)$ line were extracted for 5 different Reynolds numbers in the range [25000, 60000] while along the $L_2(X = 2.5W, Y = 0, Z)$ line, measurements were obtained only for the maximum Reynolds number ($Re = 60000$). So, the results pertaining to L_1 line (4th building) are of interest here. The time-averaged velocity and turbulence intensity profiles for the case with and without passive grid are given in Figure 21. (a) Time-average non-dimensional (streamwise) velocity and (b) turbulence intensity profiles for 5 different Reynolds numbers in the range [25000, 60000], along the $L_1(X = -0.5W, Y = 0, Z)$ line shown in Figure 7a (located at the center of the 4th building's roof). The results pertain to the case with the passive grid of Figure 1c. Hot-wire measurements were performed only in the wind tunnel of NTUA. and Figure 22, respectively. As can be seen in the following figures, the non-dimensional velocity and turbulence intensity profiles collapse, indicating that Reynolds independence is achieved for $Re > 25000$.

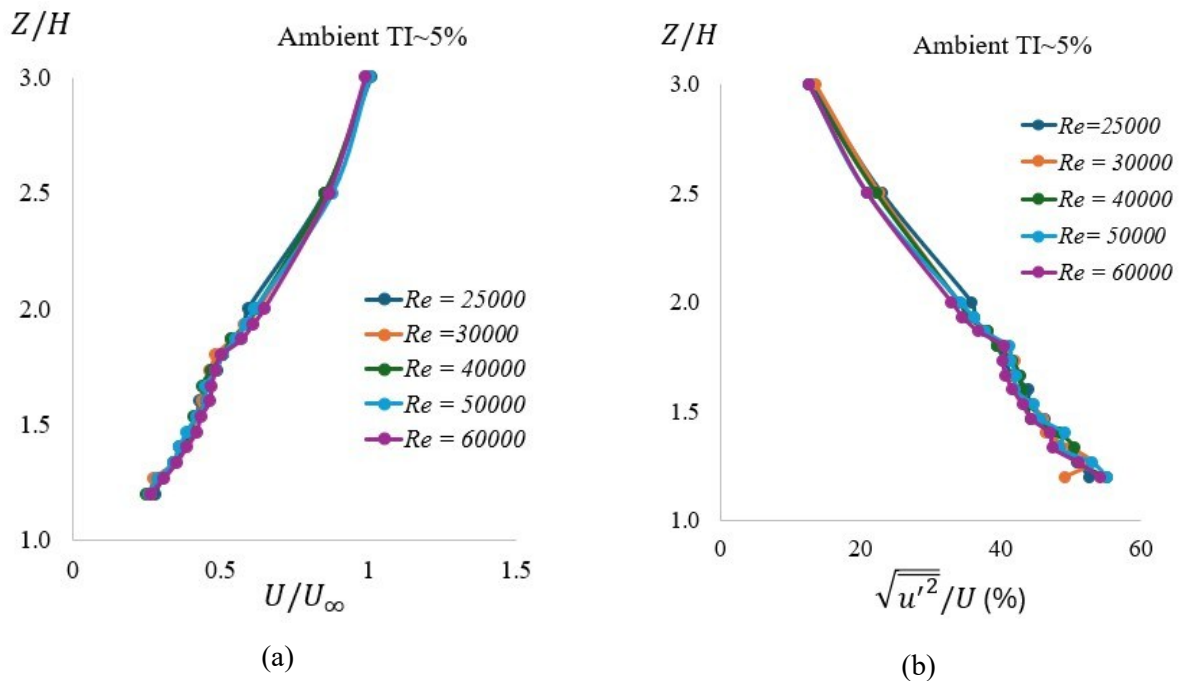


Figure 21. (a) Time-average non-dimensional (streamwise) velocity and (b) turbulence intensity profiles for 5 different Reynolds numbers in the range [25000, 60000], along the $L_1(X = -0.5W, Y = 0, Z)$ line shown in Figure 7a (located at the center of the 4th building's roof). The results pertain to the case with the passive grid of Figure 1c. Hot-wire measurements were performed only in the wind tunnel of NTUA.

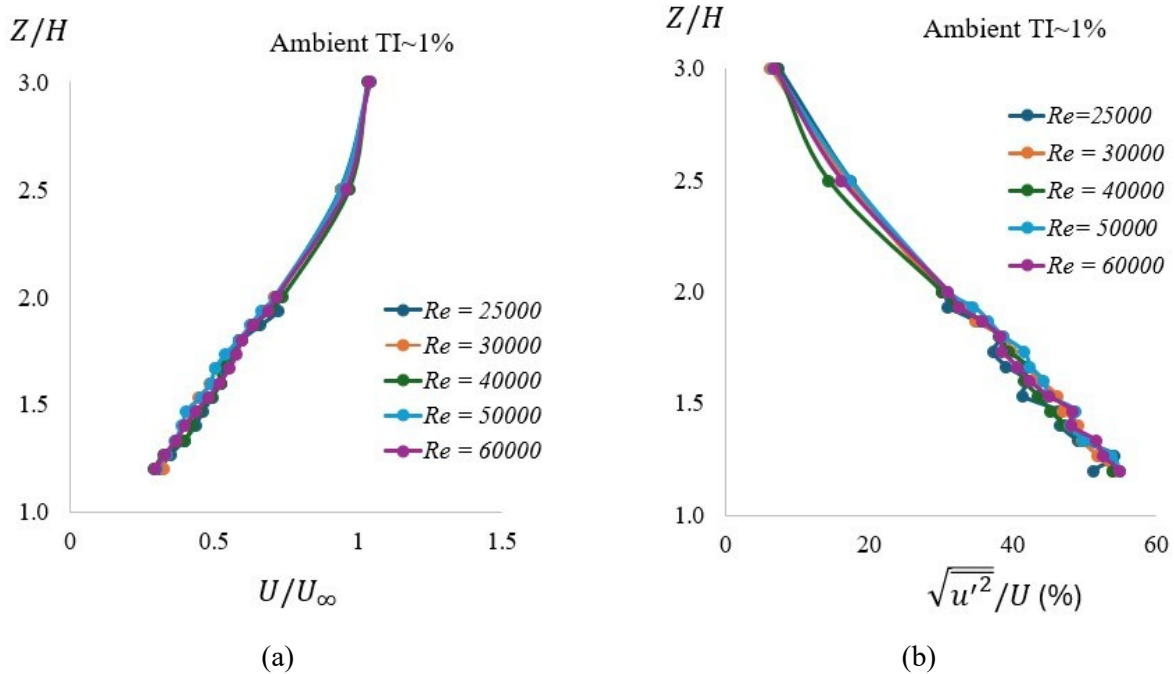


Figure 22. (a) Time-average non-dimensional (streamwise) velocity and (b) turbulence intensity profiles for 5 different Reynolds numbers in the range [25000, 60000], along the L_1 ($X = -0.5W, Y = 0, Z$) line shown in Figure 7a (located at the center of the 4th building’s roof). The results pertain to the case without the passive grid. Hot-wire measurements were performed only in the wind tunnel of NTUA.

4.3.2 Pressure measurements

Surface pressure coefficients are shown in Figure 23. for both experiments, measured along the red line of Figure 6, for different Reynolds numbers in the range [25000, 100000]. S/H accounts for the non-dimensional distance along the aforementioned line, in the direction of the flow. The static pressure of the undisturbed/free-stream flow, measured with a Pitot tube, is used as reference pressure for both experiments. The dynamic pressure at the same position is used for the calculation of the pressure coefficient C_p . The spread between the curves of different Reynolds numbers is significantly larger for the dataset acquired in Delft, especially for the upstream wall and the roof. For the downstream wall and for both datasets, this spread is at its minimum. For the dataset acquired at TU Delft, convergence seems to occur above $Re = 80000$. Interestingly though, the curves corresponding to $Re = 30000$ and $Re = 40000$ almost coincide. The differences are pronounced mainly in the range $Re \in (40000, 80000)$ before the occurrence of Reynolds number independence ($Re \geq 80000$). For the dataset acquired at NTUA, Reynolds number independence is widely achieved even for $Re > 40000$. However, for the upstream wall “batches” of coinciding curves e.g. $Re = 50000 - 60000$ and $Re = 80000 - 90000$ are encountered. Finally, for the same dataset, it is observed that Reynolds number independence is locally satisfied as soon as $Re = 25000$ e.g. at the point of the largest suction (first pressure tap of the roof). The quantitative and qualitative differences between NTUA and TU Delft datasets can only be explained in conjunction with the upcoming PTV results, showing a drastically different flow structure between the two experiments.

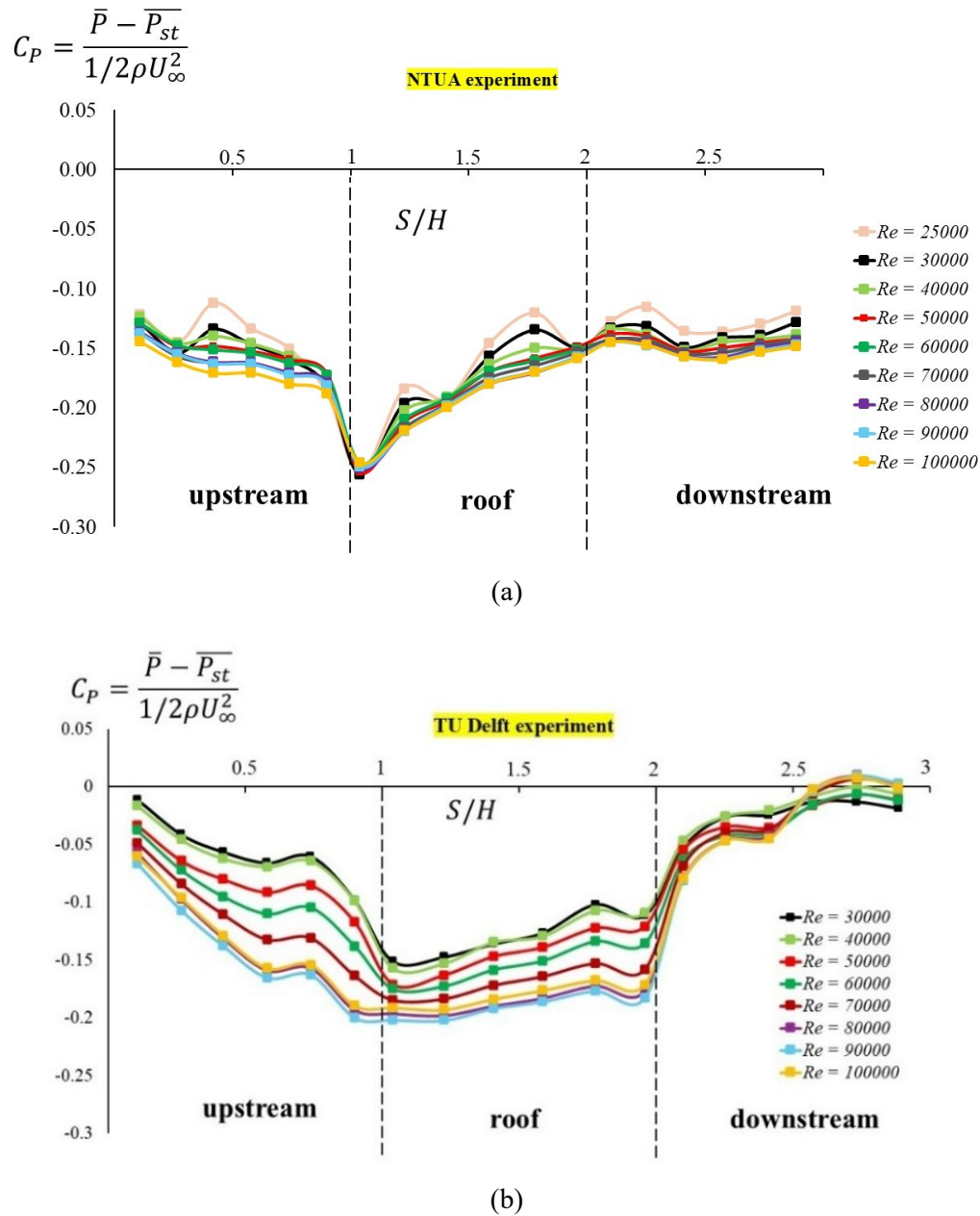


Figure 23. Surface pressure coefficient profiles for different Reynolds numbers within the range: (a) [25000, 100000] (NTUA experiment) and (b) [30000, 100000] (TU Delft experiment).

4.3.3 PTV measurements

The focus in this section is mainly on the scaling effects present in both experiments and not on the direct quantitative comparison between the two datasets. For this reason, scaling effects will be examined firstly for the NTUA experiment and then for the TU Delft one. It is clarified that for the NTUA experiment, results at different Reynolds numbers are also available for higher ambient

turbulence intensity (by using the passive grid of Figure 1c). However, an analysis of the scaling effects on the flow of the latter case is not shown here.

NTUA experiment

Contours of the normalised mean streamwise velocity component and velocity vectors are given for $Re = 25000$ and $Re = 60000$, in Figure 24 for the centre-plane ($Y/H = 0$, see Figure 7) of the examined canyon at NTUA. Overall, no significant differences are obvious between the results of $Re = 25000$ and $Re = 60000$, except: (i) some small differences in the lower left corner where the secondary vortex is observed, (ii) for the higher Re number, there is a slightly stronger upward velocity component near the upper corner of the leeward wall of the canyon and (iii) the region of the most negative streamwise velocity (dark blue contour level) is smaller at $Re = 25000$. This was also corroborated by examining velocity and turbulent kinetic energy profiles at three different positions of the plane of symmetry i.e. $X/H = 0.5$ (centre), $X/H = 0.003$ (leeward wall) and $X/H = 0.98$ (windward wall) for all available Re numbers. In this way, Reynolds number independence is also verified in a more quantitative manner. The results are given in

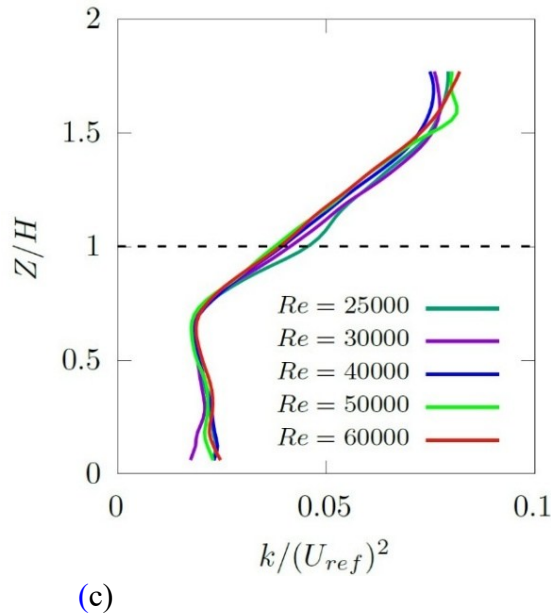


Figure 25. Figure 26. and Figure 27. , respectively. It should be mentioned that the spread of W/U_{ref} curves is mostly of the same order as the uncertainty levels shown in Figure 19. The differences though of W/U_{ref} from $Re = 40000$ to $Re = 60000$ in Figure 27. are such that they cannot be attributed solely to uncertainty, especially around $Z/H = 0.5$. This conclusion is in good qualitative agreement with the surface pressure results of Figure 23. a, since around $S/H = 0.5$ (i.e. $Z/H = 0.5$ of the windward wall) there is also a non-negligible spread between the presented curves. Local convergence of the surface pressure curves (Figure 23. a) around $S/H = 1$ and $S/H = 2$ (i.e. around the sharp edges of the roof) is also in accordance with the behaviour at $Z/H \approx 1$, observed in Figure 27. and Figure 26. , respectively.

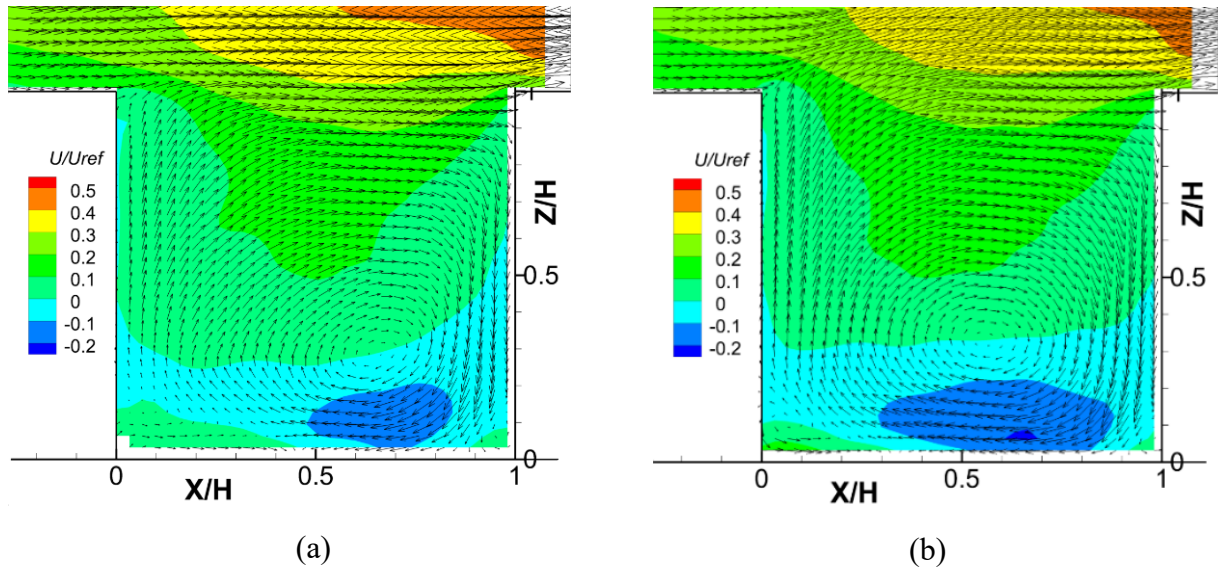
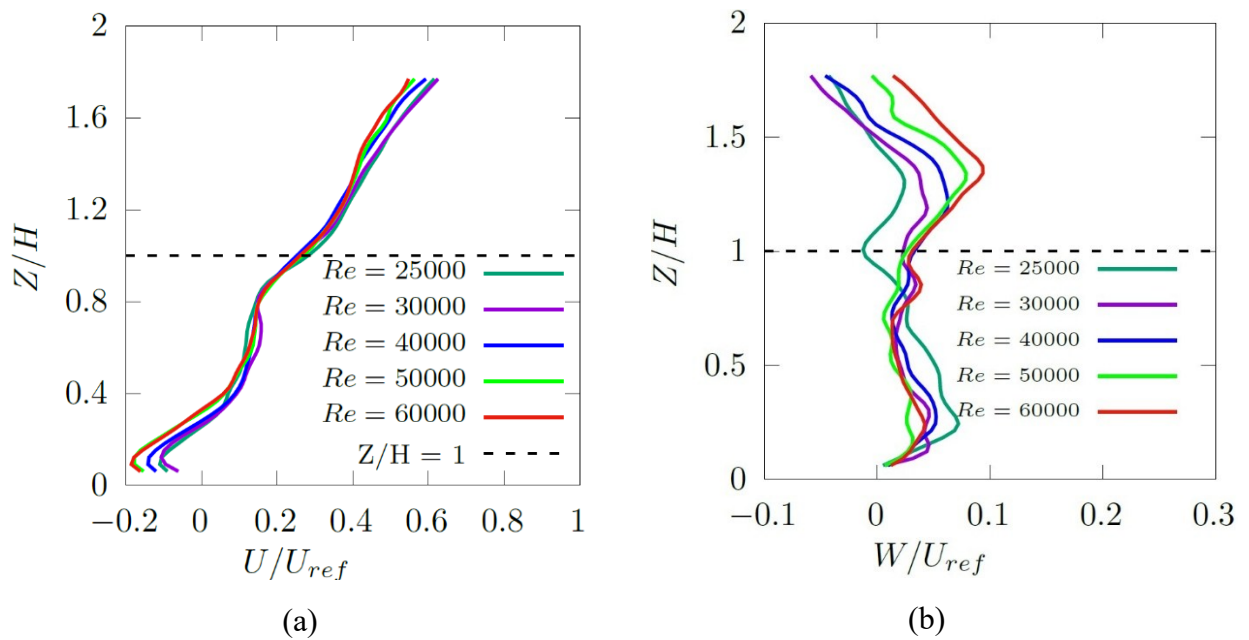
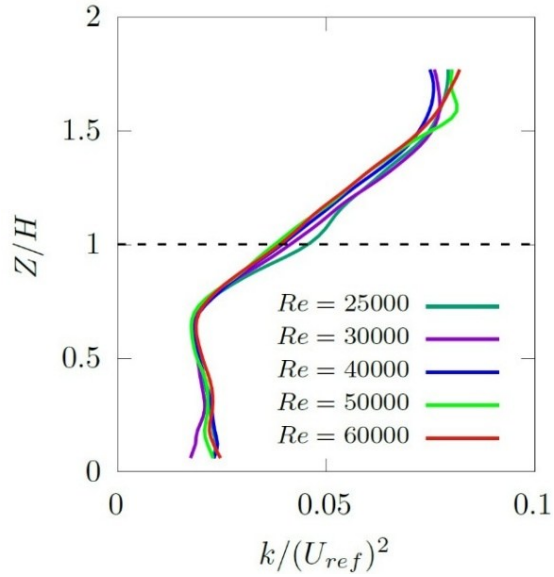


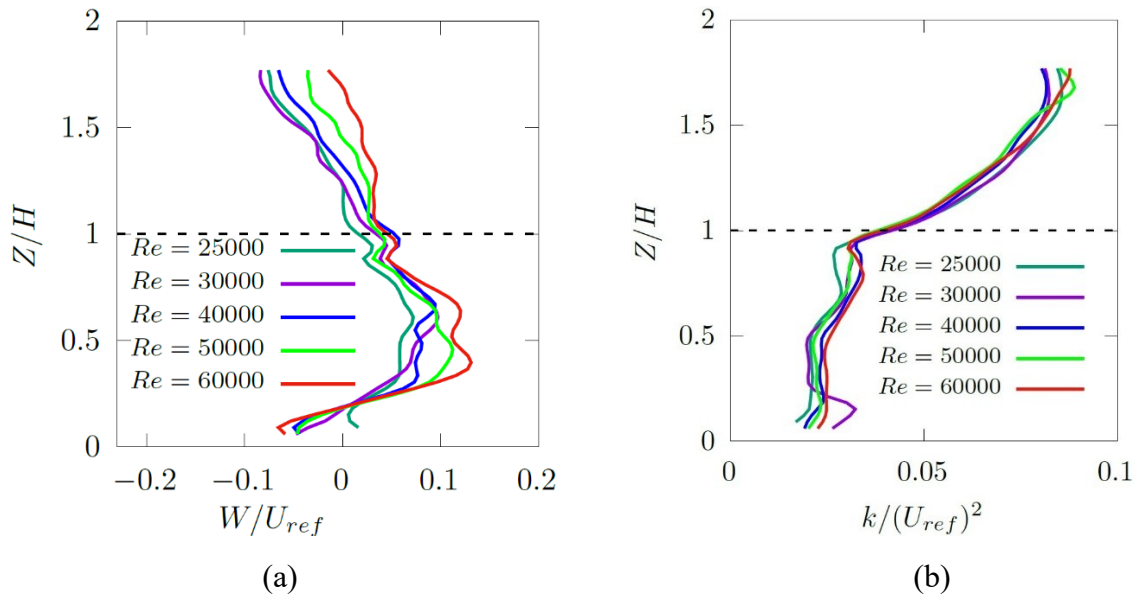
Figure 24. Velocity vectors (tangent) and contours of the normalised mean streamwise velocity component U/U_{ref} for: (a) $Re = 25000$ and (b) $Re = 60000$, in the centre-plane. The flow is from left to right, with $U_{ref} = U_{\infty}$.





(c)

Figure 25. Profiles of the non-dimensional: (a) mean streamwise velocity (U/U_{ref}), (b) mean vertical velocity (W/U_{ref}) and (c) turbulent kinetic energy (k/U_{ref}^2) for $Re \in [25000, 60000]$ at $X/H = 0.5$ and $Y/H = 0$, with $U_{ref} = U_{\infty}$.



(a)

(b)

Figure 26. Profiles of the non-dimensional: (a) mean vertical velocity (W/U_{ref}) and (b) turbulent kinetic energy (k/U_{ref}^2) for $Re \in [25000, 60000]$ at $X/H = 0.003$ (leeward wall) and $Y/H = 0$, with $U_{ref} = U_{\infty}$.

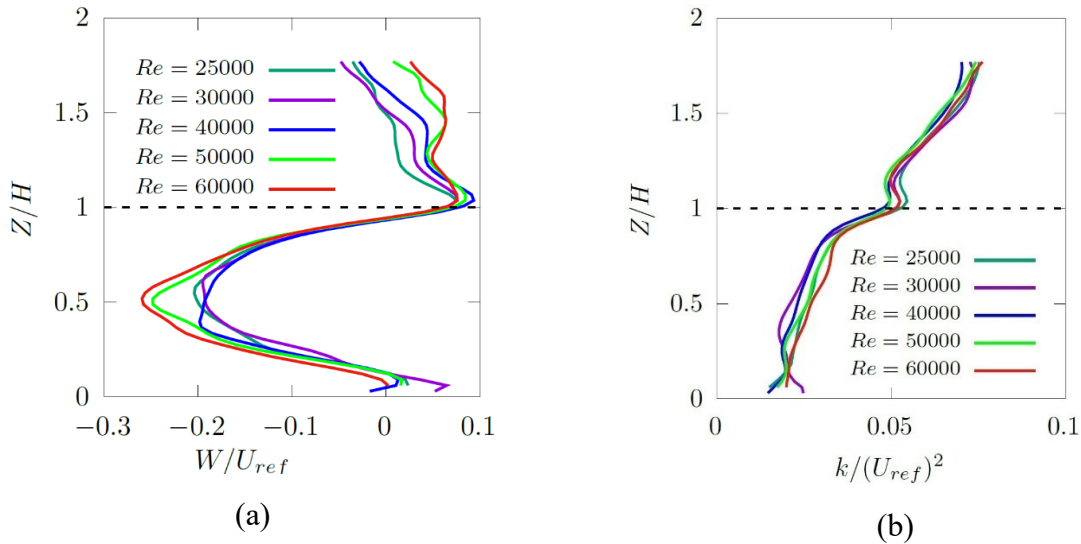


Figure 27. Profiles of the non-dimensional: (a) mean vertical velocity (W/U_{ref}) and (b) turbulent kinetic energy (k/U_{ref}^2) for $Re \in [25000, 60000]$ at $X/H = 0.98$ (windward wall) and $Y/H = 0$, with $U_{ref} = U_{\infty}$.

A similar analysis is done also for a plane near the one end of the street canyon (edge of the canyon) which belongs to the measurement volume. This plane is located at $Y/H = 3.5$ i.e. half a canyon’s height/width away from the edge of the canyon. Contours of the normalised mean lateral velocity component (V/U_{ref}) and velocity vectors are given for $Re = 25000$ and $Re = 60000$, in [Figure 28](#). . Negative values of V/U_{ref} point inwards i.e. towards the central region of the canyon. No significant differences are obvious between the results of $Re = 25000$ and $Re = 60000$. This was again verified by examining velocity and turbulent kinetic energy profiles but only at $X/H = 0.5$ (centre), shown in [Figure 29](#). .

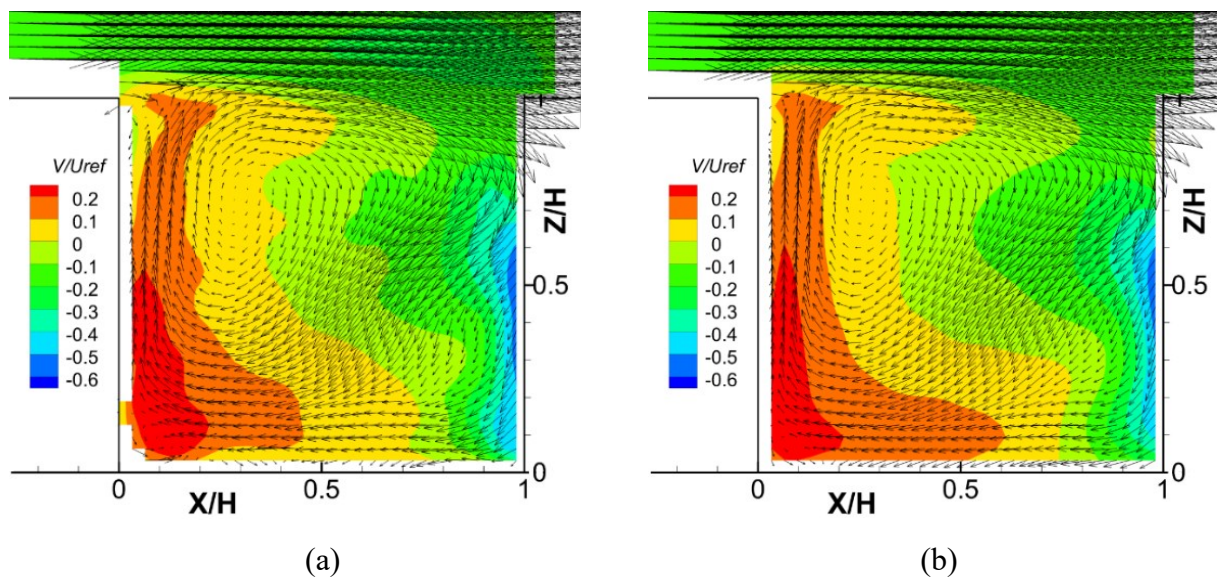


Figure 28. Velocity vectors (tangent) and contours of the normalised mean lateral velocity component V/U_{ref} for: (a) $Re = 25000$ and (b) $Re = 60000$, in the plane located at $Y/H = 3.5$ (half a canyon's height/width away from the edge of the canyon). The flow is from left to right, with $U_{ref} = U_{\infty}$. Negative values of V/U_{ref} point inwards i.e. towards the central region of the canyon.

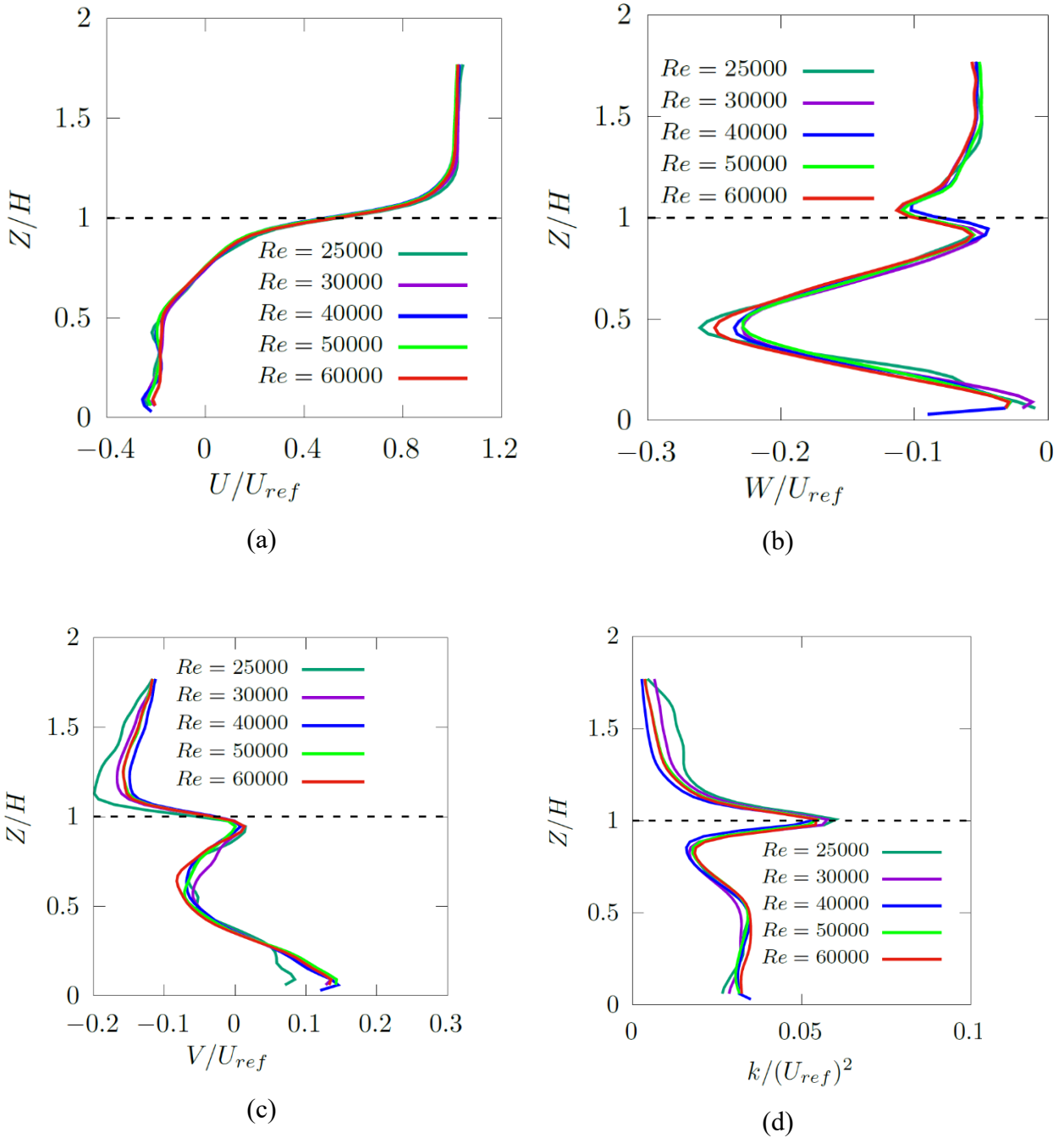


Figure 29. Profiles of the non-dimensional: (a) mean streamwise velocity (U/U_{ref}), (b) mean vertical velocity (W/U_{ref}), (c) mean lateral velocity (V/U_{ref}) and (d) turbulent kinetic energy (k/U_{ref}^2) for $Re \in [25000, 60000]$ at $X/H = 0.5$ and $Y/H = 3.5$, with $U_{ref} = U_{\infty}$.

TU Delft experiment

Following the same reasoning as above for the NTUA experiment, contours of the normalised mean streamwise velocity component and velocity vectors are given for $Re = 30000$ and $Re = 100000$, in [Figure 30](#). for the centre-plane ($Y/H = 0$, see [Figure 7](#)) of the examined canyon. There are two noticeable differences between the results of $Re = 30000$ and $Re = 100000$: (i) the recirculation above the roof of the upstream building seems to be less extensive for $Re = 30000$ than $Re = 100000$ and (ii) the flow exhibits higher non-dimensional streamwise velocities for $Re = 30000$ than $Re = 100000$, for the same height.

It should be noted that the flow structure between the NTUA and TU Delft experiments is drastically different i.e. in the former case ([Figure 24](#).) there is a vortex while in the latter case there is not one ([Figure 30](#).). New experiments (not presented here) being performed by the partners at TU Delft indicate that the existence of a (decreasing) pressure gradient in the streamwise direction may be the prerequisite condition in order for the canyon vortex to be present. Of course, this streamwise pressure gradient is non-negligible in the enclosed test section of NTUA, while being near zero in the OJF of TU Delft. The static pressure drop as a percentage of the dynamic pressure in the wind tunnel of NTUA reached a maximum of 9% for $Re = 25000$. The latter value corresponds to the difference between the measured static pressure upstream of the whole model (i.e. upstream of all the canyons) and that measured exactly above the examined canyon. Both pressures were measured in the undisturbed, free-stream flow region.

Reynolds number independence for $Re \geq 30000$ was also examined by means of velocity and turbulent kinetic energy profiles at three different positions of the plane of symmetry i.e. $X/H = 0.5$, $X/H = 0.07$ and $X/H = 0.93$ for all available Re numbers. In this way, Reynolds number independence is also verified in a more quantitative manner. The results are given in



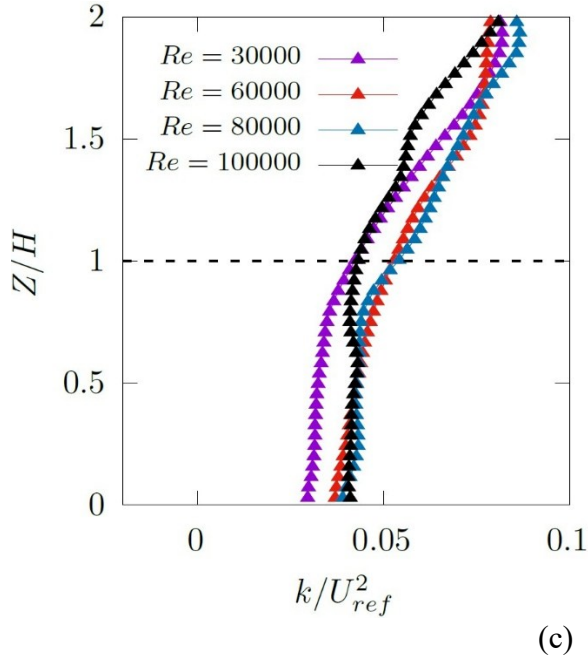


Figure 31. Figure 32. and Figure 33. , respectively.

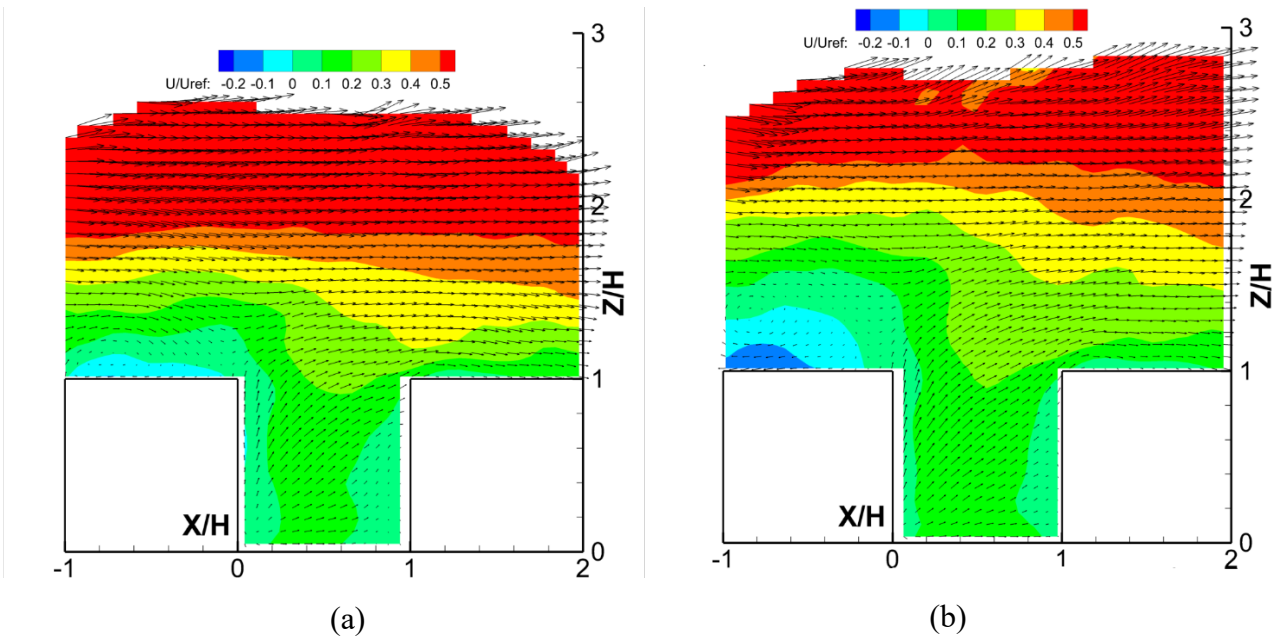


Figure 30. Velocity vectors (tangent) and contours of the normalised mean streamwise velocity component U/U_{ref} for: (a) $Re = 30000$ and (b) $Re = 100000$, in the centre-plane. The flow is from left to right, with $U_{ref} = U_{\infty}$.

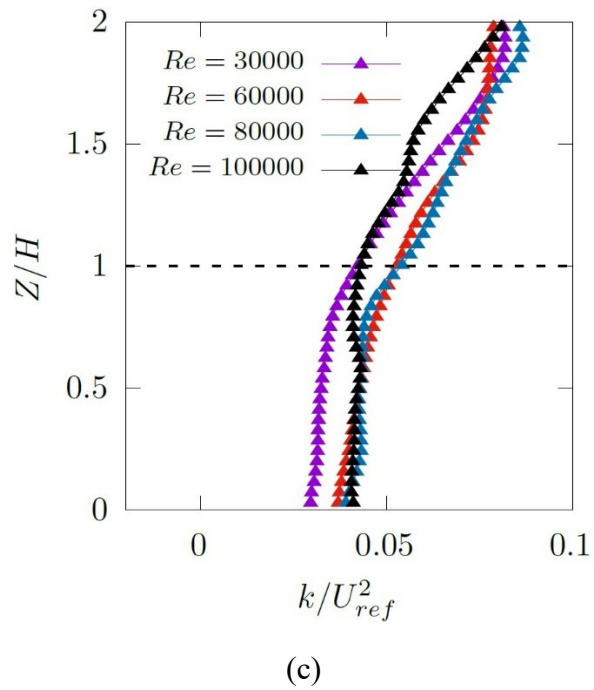
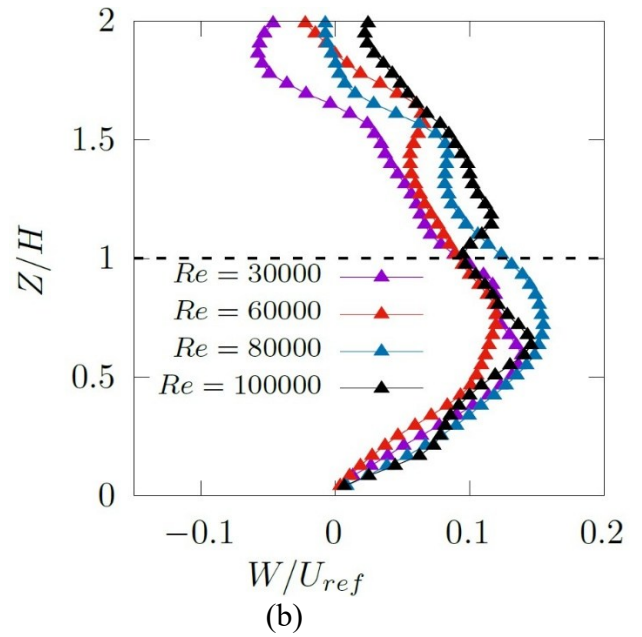
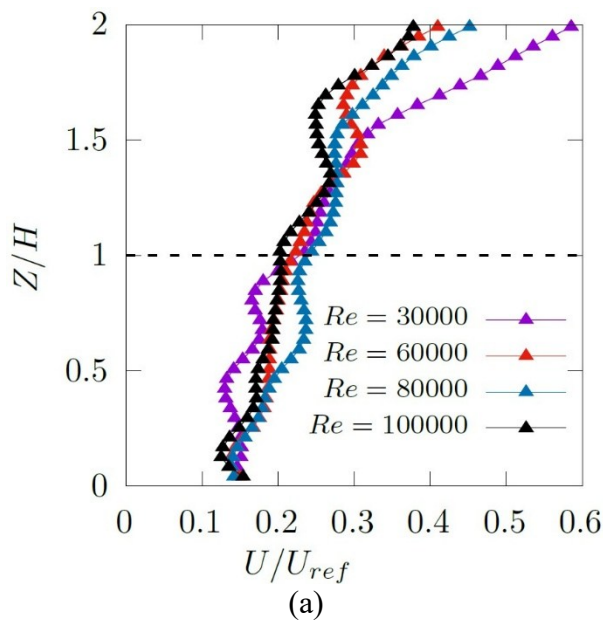


Figure 31. Profiles of the non-dimensional: (a) mean streamwise velocity (U/U_{ref}), (b) mean vertical velocity (W/U_{ref}) and (c) turbulent kinetic energy (k/U_{ref}^2) for $Re \in [30000, 100000]$ at $X/H = 0.5$ and $Y/H = 0$, with $U_{ref} = U_{\infty}$.

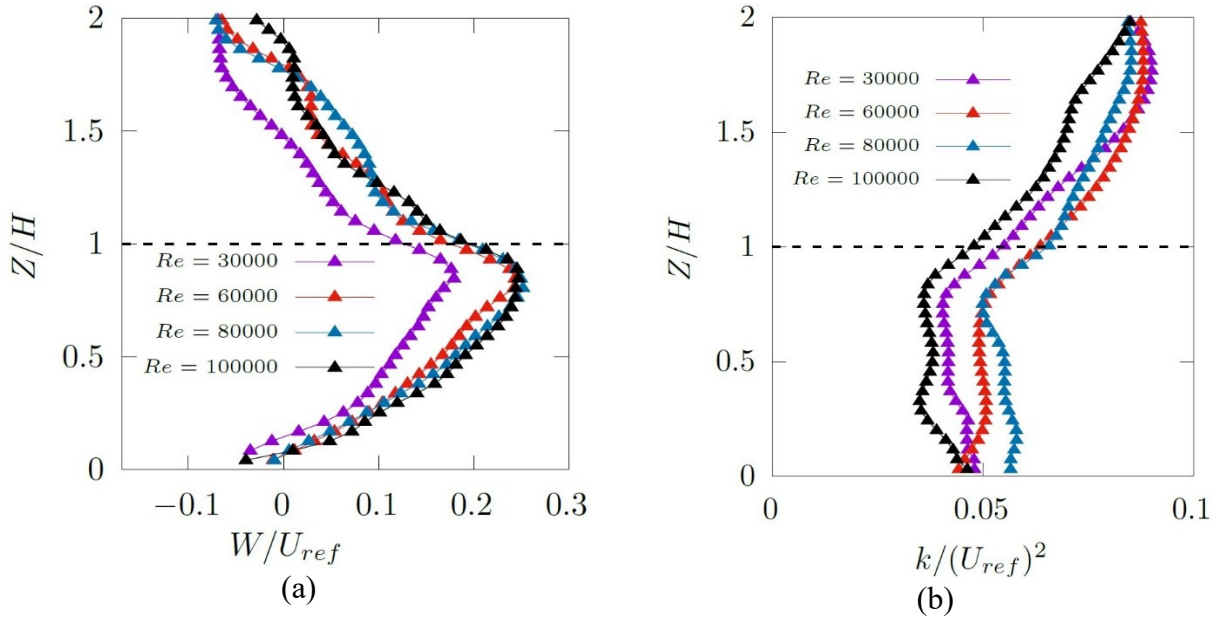


Figure 32. Profiles of the non-dimensional: (a) mean vertical velocity (W/U_{ref}) and (b) turbulent kinetic energy (k/U_{ref}^2) for $Re \in [30000, 100000]$ at $X/H = 0.07$ and $Y/H = 0$, with $U_{ref} = U_{\infty}$.

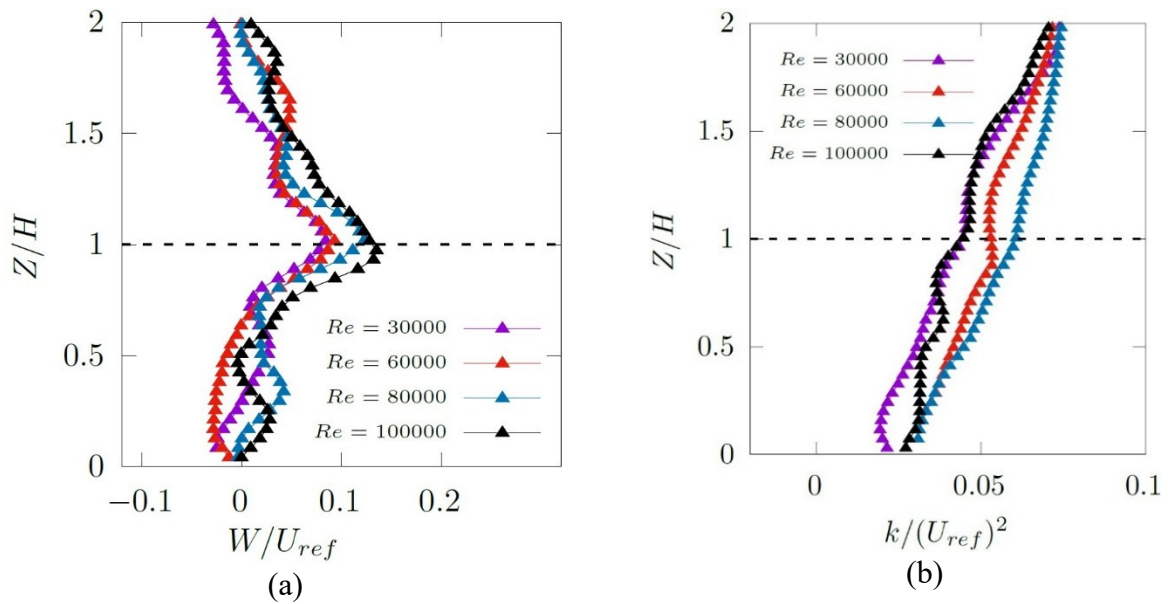


Figure 33. Profiles of the non-dimensional: (a) mean vertical velocity (W/U_{ref}) and (b) turbulent kinetic energy (k/U_{ref}^2) for $Re \in [30000, 100000]$ at $X/H = 0.93$ and $Y/H = 0$, with $U_{ref} = U_{\infty}$.

A similar analysis to the one conducted for the centre-plane is also presented for a plane near one end of the street canyon, within the measurement volume., i.e. at $Y/H = 3.5$ i.e. half a canyon’s height/width away from the edge of the canyon. In particular, contours of the normalised mean lateral velocity component (V/U_{ref}) and velocity vectors are given for $Re = 30000$ and $Re = 100000$, in **Figure 34.** . Negative values of V/U_{ref} point inwards i.e. towards the central region of the canyon. No significant differences are obvious between the results of $Re = 30000$ and $Re = 100000$ except the fact that the region of negative V/U_{ref} velocities (incoming flow), near the windward wall of the canyon, is more extensive in the case of $Re = 30000$. An interesting observation is that the flow structure at this plane is similar to the one encountered in **Figure 28.** , pertaining to the NTUA experiment. Hence, the differences between the two datasets seem to be significantly reduced as one approaches the lateral end of the canyon (i.e. as Y increases). Velocity and turbulent kinetic energy profiles are once again illustrated but only at $X/H = 0.5$ (centre), shown in **Figure 35.** .

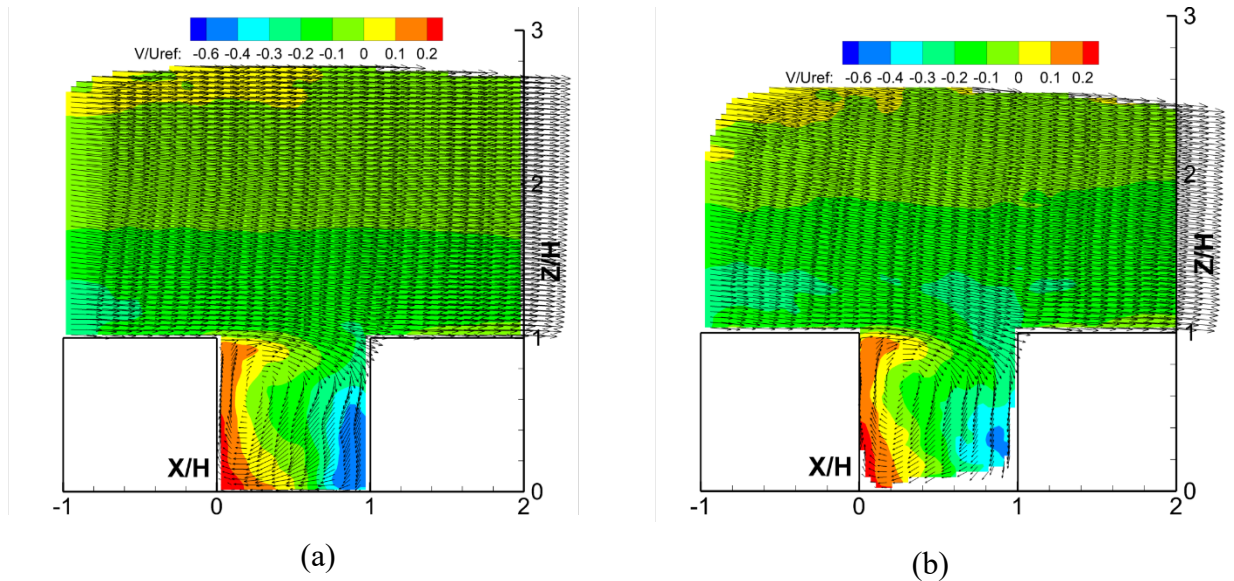


Figure 34. Velocity vectors (tangent) and contours of the normalised mean lateral velocity component V/U_{ref} for: (a) $Re = 30000$ and (b) $Re = 100000$, in the plane located at $Y/H = 3.5$ (half a canyon’s height/width away from the edge of the canyon). The flow is from left to right, with $U_{ref} = U_{\infty}$. Negative values of V/U_{ref} point inwards i.e. towards the central region of the canyon.

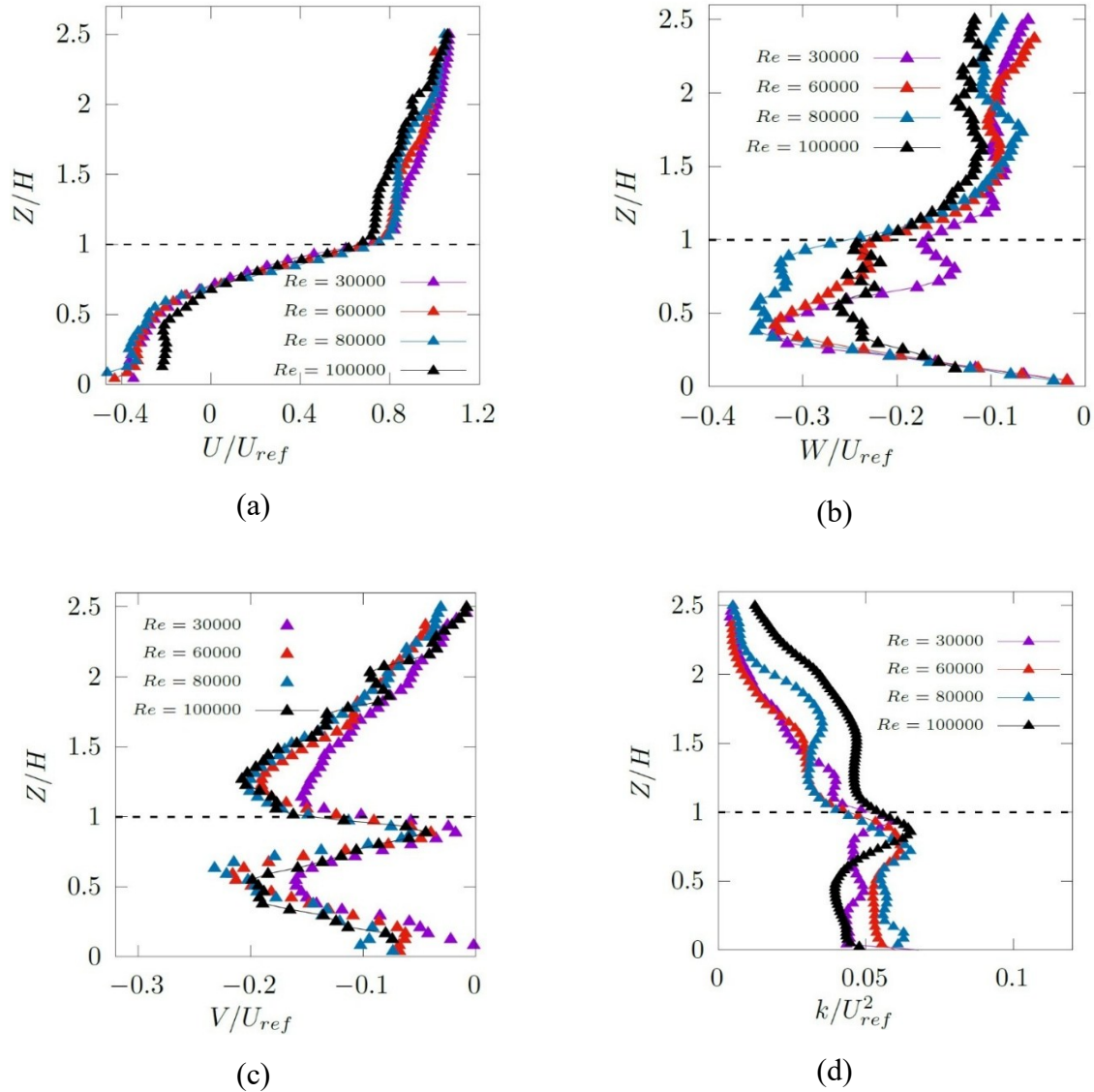


Figure 35. Profiles of the non-dimensional: (a) mean streamwise velocity (U/U_{ref}), (b) mean vertical velocity (W/U_{ref}), (c) mean lateral velocity (V/U_{ref}) and (d) turbulent kinetic energy (k/U_{ref}^2) for $Re \in [30000, 100000]$ at $X/H = 0.5$ and $Y/H = 3.5$, with $U_{ref} = U_{\infty}$.

4.4 Effects of vegetation

As already mentioned, two different types of vegetation (Figure 9) have been tested in the framework of this twin test: (a) roof greening on both buildings comprising the examined street canyon and (b) a hedge row positioned equidistantly from the walls of the buildings comprising the examined canyon, along its lateral (Y) axis. In this section, a comparison between the bare canyon case and the other two configurations is effectuated for the NTUA dataset and for the case without the passive grid (low ambient turbulence intensity). It is worth mentioning that both types of vegetation were also tested for the higher ambient turbulence case and the corresponding dataset is

available for future analysis. The experiments pertaining to the low ambient turbulence intensity were repeated at TU Delft, but the respective results are not shown here. These experiments were performed only at $Re = 60000$ in the wind tunnel of NTUA, whereas in the OJF of TU Delft, measurements were conducted at $Re = 40000, 60000$ and 80000 (see section 4.1). Firstly, contours of the normalised mean streamwise velocity component along with velocity vectors are given for the centre-plane ($Y/H = 0$, see Figure 7) of the examined canyon and for the: (a) bare canyon configuration, (b) configuration with roof greening and (c) configuration with hedge row at $Re = 60000$, in Figure 36. .

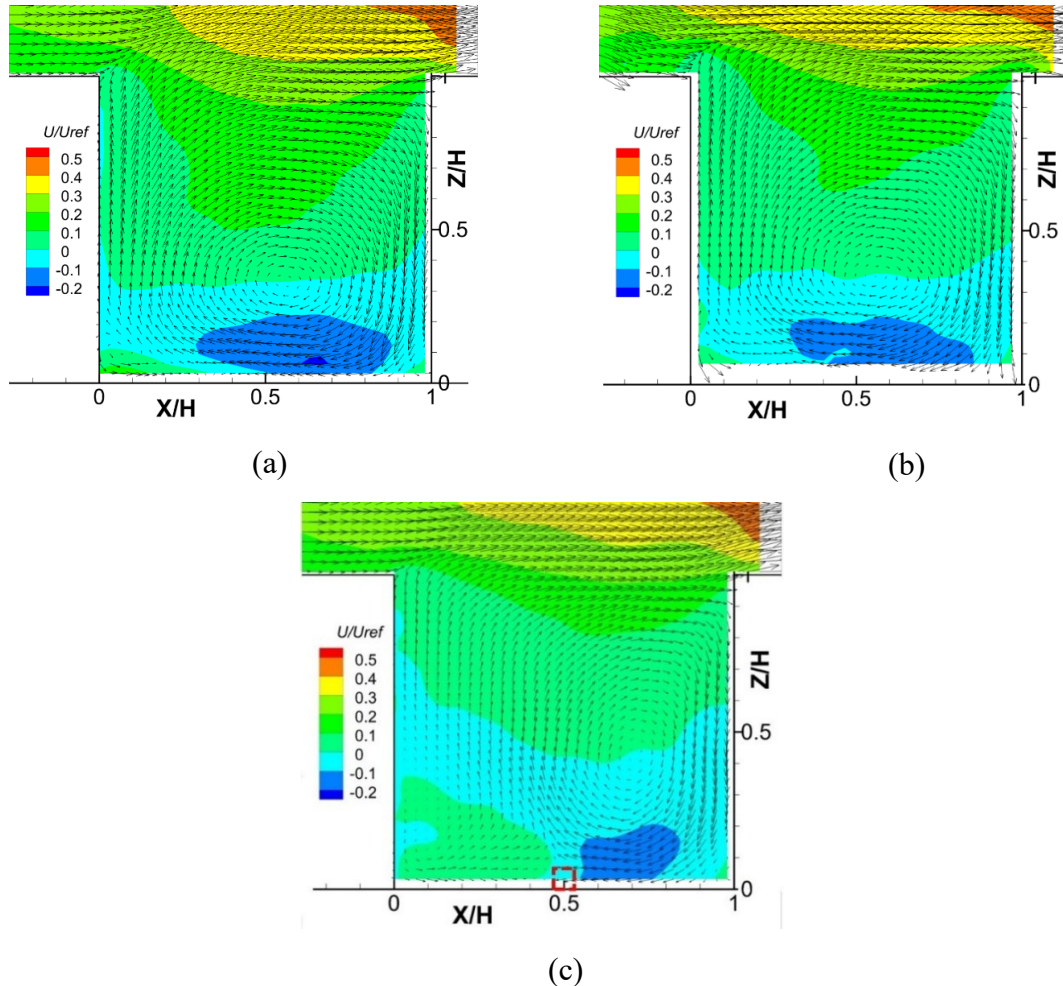


Figure 36. Velocity vectors (tangent) and contours of the normalised mean streamwise velocity component U/U_{ref} in the centre-plane ($Y/H = 0$) of the canyon, for the: (a) bare canyon case, (b) configuration with roof greening and (c) configuration with the hedge row where the latter is indicated by the red dashed box. The flow is from left to right and the Reynolds number is equal to 60000 for all cases, with $U_{ref} = U_{\infty}$.

It is observed that the influence of roof greening on the flow inside the canyon is almost negligible. This is not the case though for the configuration with the hedge row. More specifically, the flow structure is clearly different from that of the bare canyon case since: (i) the position and the

shape of the main canyon vortex changes under the influence of the hedge row and (ii) the secondary vortex in the lower left corner is clearly larger for the hedge row configuration. Conclusively, this type of vegetation “separates” the flow into two distinctive vortical structures, i.e. one upstream of the hedge row (indicated by the red dashed box) and another one downstream of it.

Similar results are given in Figure 37. but for the plane located at $Y/H = 3.5$ i.e. half a canyon’s height/width away from the edge of the canyon. Contours of the mean lateral velocity component V/U_{ref} along with velocity vectors are given for the: (a) bare canyon configuration, (b) configuration with roof greening and (c) configuration with hedge row at $Re = 60000$.

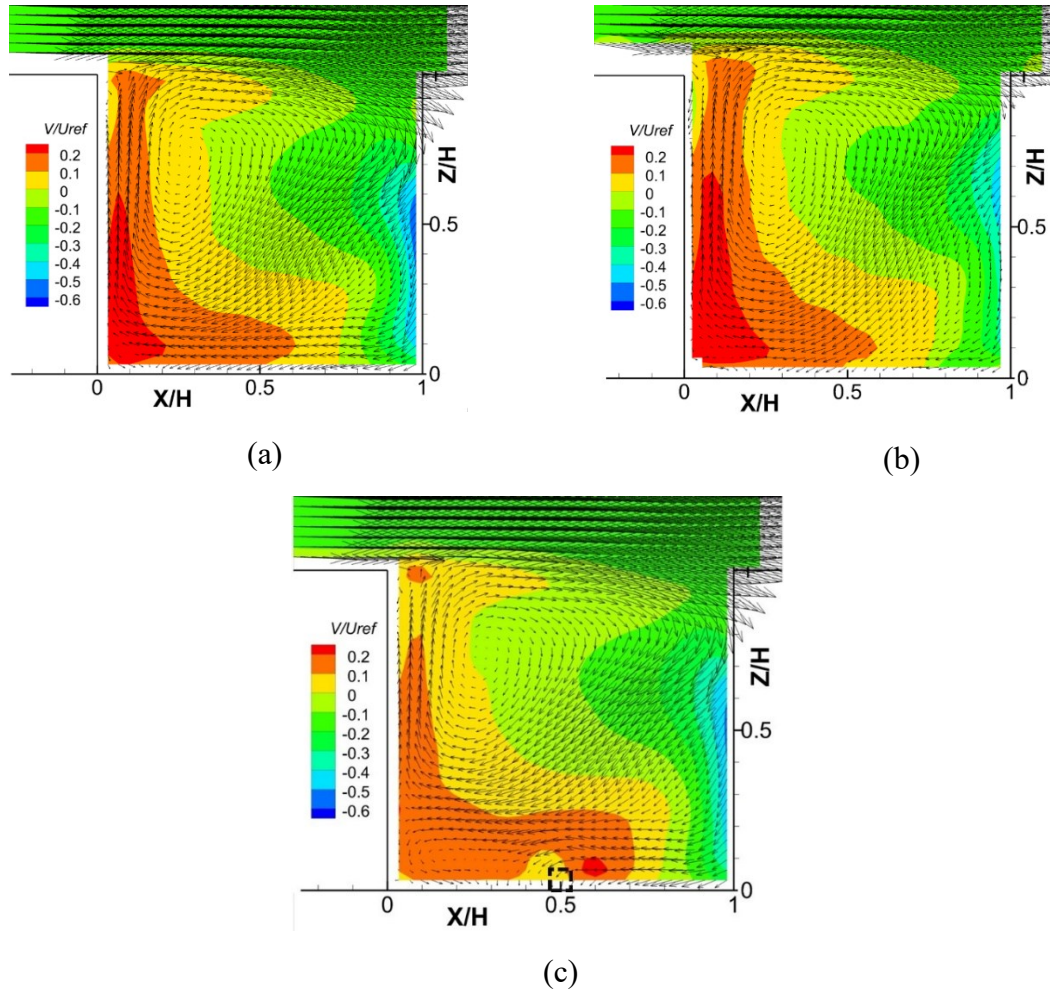


Figure 37. Velocity vectors (tangent) and contours of the normalised mean lateral velocity component V/U_{ref} for the: (a) bare canyon case, (b) configuration with roof greening and (c) configuration with the hedge row (indicated by the black dashed box), in the plane located at $Y/H = 3.5$ (half a canyon’s height/width away from the edge of the canyon). The flow is from left to right and the Reynolds number is equal to 60000 for all cases, with $U_{ref} = U_{\infty}$. Negative values of V/U_{ref} point inwards i.e. towards the central region of the canyon.

Again, the roof greening has no significant influence on the flow inside the canyon as it is observed by comparing Figure 37. a with Figure 37. b. The only exception is near the windward wall

of the canyon ($X/H \approx 1$), where negative V/U_{ref} velocities of lower magnitude are observed for the roof greening configuration. This means that the incoming airflow from the lateral side of the canyon is of lower velocity, since negative values of V/U_{ref} point inwards i.e. towards the central region of the canyon. Furthermore, even the tangent vectors ($\vec{U} + \vec{V}$) are clearly influenced by the presence of roof greening, in terms of both inclination and size (proportional to $|\vec{U} + \vec{V}|$) in the region adjacent to the windward wall. The effect of the hedges on the flow structure is quite clear, especially near the lower left corner of the canyon, where a secondary vortex is observed.

4.5 Influence of free-stream turbulence

4.5.1 Hot-wire measurements

Hot-wire measurements were performed in the wind tunnel of NTUA for the cases with (see Figure 1c) and without the passive grid (i.e. for higher and lower ambient turbulence intensity, respectively) along the lines $L_1(X = -0.5W, Y = 0, Z)$ and $L_2(X = 2.5W, Y = 0, Z)$ (Figure 7a) at $Re = 60000$. The time-average velocity and turbulence intensity profiles along the lines L_1 (4th building) and L_2 (5th building) are given in Figure 38. and Figure 39. , respectively. The influence of free stream turbulence is mostly pronounced above $Z/H = 1.5 - 2$.

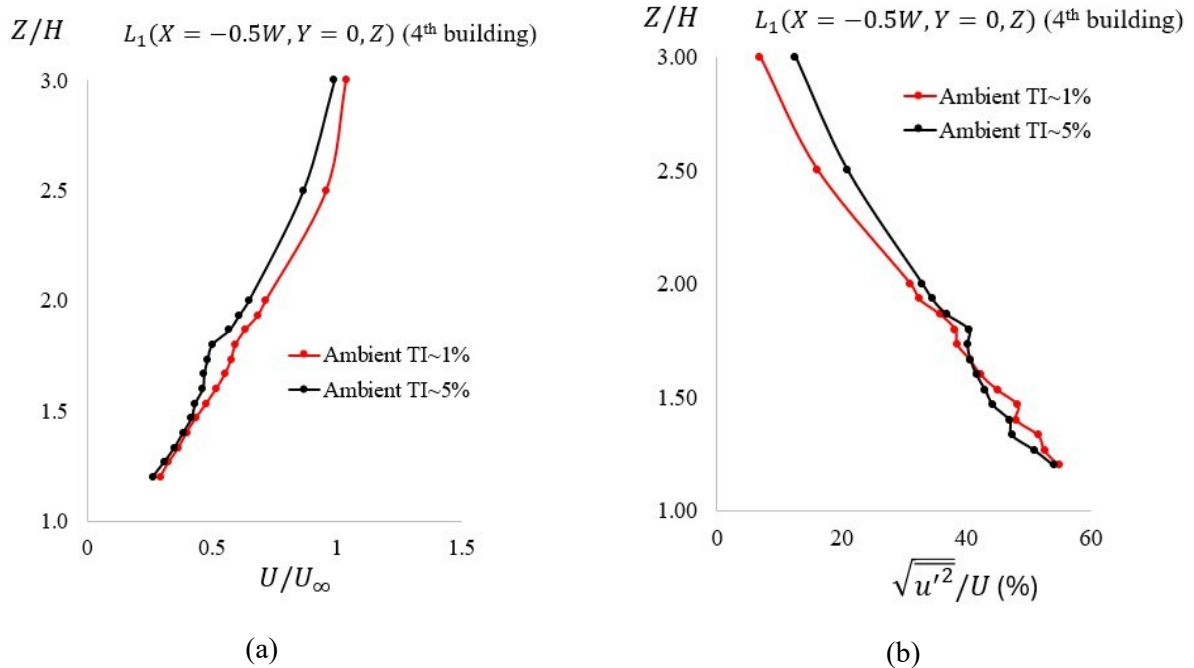


Figure 38. (a) Time-average non-dimensional (streamwise) velocity and (b) turbulence intensity profiles along the $L_1(X = -0.5W, Y = 0, Z)$ line shown in Figure 7a (located at the center of the 4th building’s roof). The black curves correspond to the case with the passive grid while the red ones to the case without it. The Reynolds number is equal to 60000. Hot-wire measurements were performed only in the wind tunnel of NTUA.

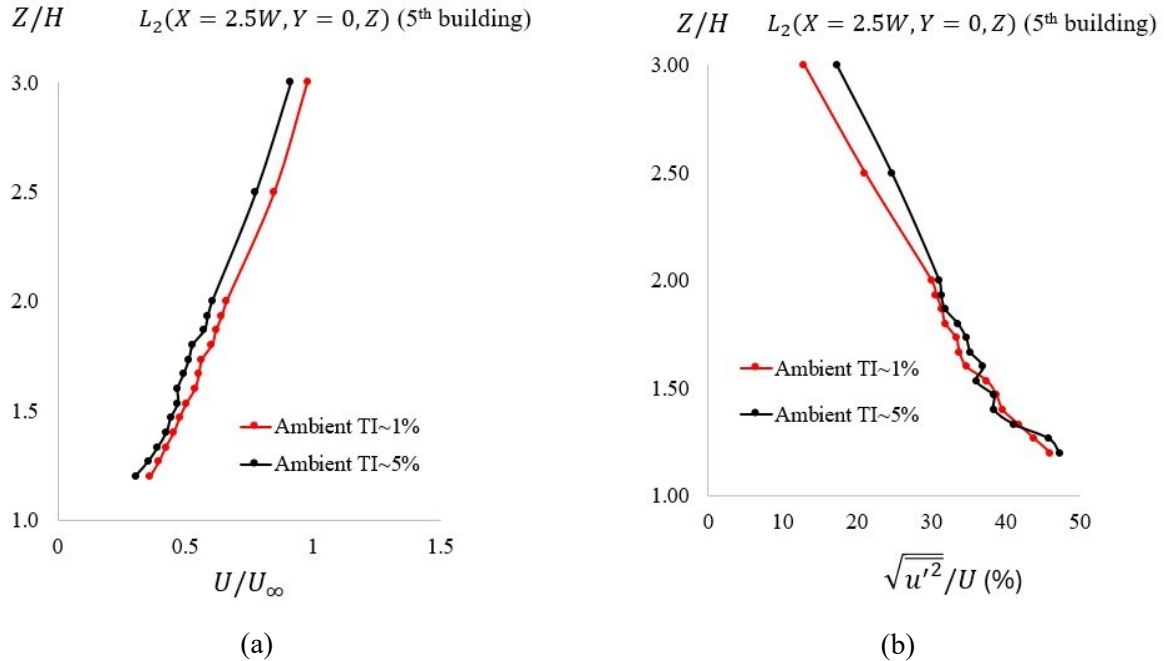


Figure 39. (a) Time-average non-dimensional velocity and (b) turbulence intensity profiles along the $L_2(X = 2.5W, Y = 0, Z)$ line shown in Figure 7a (located at the center of the 5th building’s roof). The black curves correspond to the case with the passive grid while the red ones to the case without it. The Reynolds number is equal to 60000. Hot-wire measurements were performed only in the wind tunnel of NTUA.

4.5.2 PTV measurements

Here, cases with lower (without passive grid) and higher (with passive grid) ambient turbulence intensity are compared based on the acquired PTV datasets at NTUA. It is reminded that this comparison is not pertinent to the experiment conducted at TU Delft, since only cases with low ambient turbulence intensity (~1%) were tested there. The flow in the wind tunnel of NTUA has inherently a turbulence intensity 1-2% i.e. without any passive devices (e.g. passive grid) and/or models inside the section. Firstly, contours of the normalised mean streamwise velocity component along with velocity vectors are given for the centre-plane ($Y/H = 0$, see Figure 7) and for the: (a) low turbulence case and (b) high turbulence case at $Re = 60000$ (maximum Reynolds number tested at NTUA), in Figure 40. .

The higher ambient turbulence intensity seems to influence the flow inside the canyon. The more pronounced difference between the two examined cases is the position of the canyon vortex. In particular, it is closer to the windward wall ($X/H = 1$) and closer to the ground, for the high turbulence case. Moreover, the region of negative velocities is less extensive for the case of high ambient turbulence. A more quantitative comparison consists of examining velocity and turbulent kinetic energy profiles in the centre-plane ($Y/H = 0$) of the examined canyon at $X/H = 0.5$ for both ambient turbulence scenarios. This is shown in Figure 41. Profiles of the non-dimensional: (a) mean streamwise velocity (U/U_{ref}), (b) mean vertical velocity (W/U_{ref}) and (c) turbulent kinetic energy (k/U_{ref}^2) for the low and high (dashed lines) turbulence cases at $X/H = 0.5$ and $Y/H = 0$, with $U_{ref} = U_\infty$. Results are shown for the minimum and maximum Reynolds numbers tested in the wind

tunnel of NTUA i.e. 25000 and 60000. for the minimum and maximum Reynolds numbers tested in the wind tunnel of NTUA i.e. 25000 and 60000. For the streamwise velocity, shown in Figure 41. a, there are differences near the ground for both Reynolds numbers. In the case of low ambient turbulence there are negative values of streamwise velocity in this region, opposite to the high turbulence case where its value is close to zero. This conclusion is in accordance with the observations made for Figure 40. . Regarding the vertical velocity, shown in Figure 41. b, although there are some differences, they are less than $0.05U_{ref}$ with $U_{ref} = U_{\infty}$, for both Reynolds numbers and at the same order of the differences due to scaling effects. Finally, an interesting observation is that the turbulent kinetic energy of the high turbulence case is marginally higher than that of the low turbulence one inside the canyon ($Z/H < 1$) while the opposite trend is observed outside of it. One may expect that the turbulence levels encountered near the roofs ($Z/H \approx 1 - 1.5$) of the buildings are mostly due to turbulence production from flow contact with the buildings rather than the ambient turbulence levels. Also, the existence of the “sheltering” effect [2] in canyon flows may limit the influence of the ambient turbulence on the observed turbulence levels inside the canyon ($Z/H < 1$).

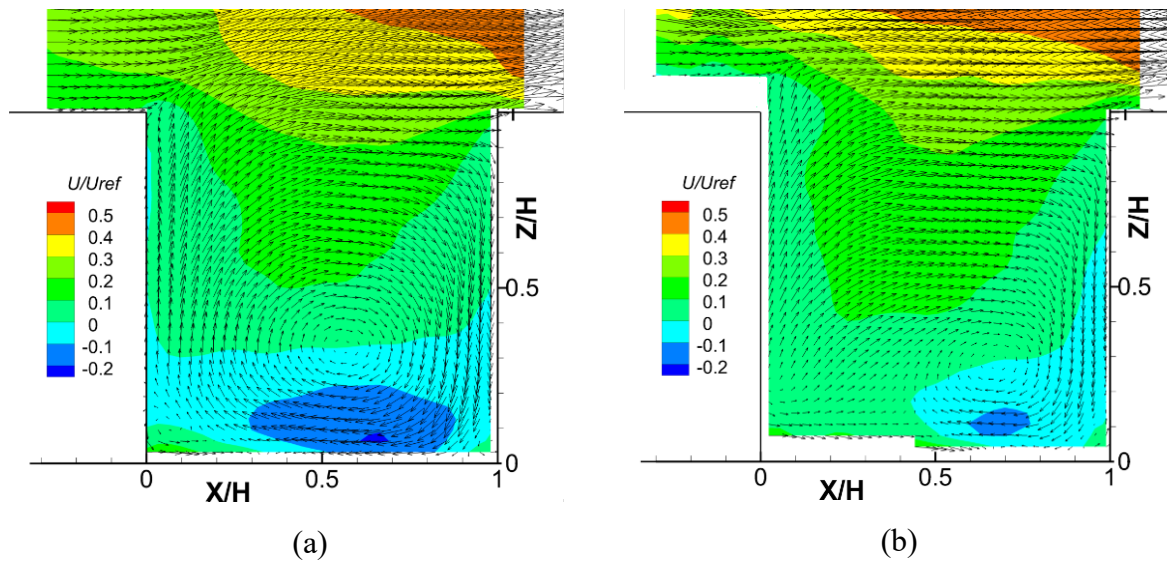


Figure 40. Velocity vectors (tangent) and contours of the normalised mean streamwise velocity component U/U_{ref} in the centre-plane ($Y/H = 0$) of the canyon, for the: (a) low turbulence case (without the passive grid), (b) high turbulence case (with the passive grid). The flow is from left to right and the Reynolds number is equal to 60000 for both figures, with $U_{ref} = U_{\infty}$.

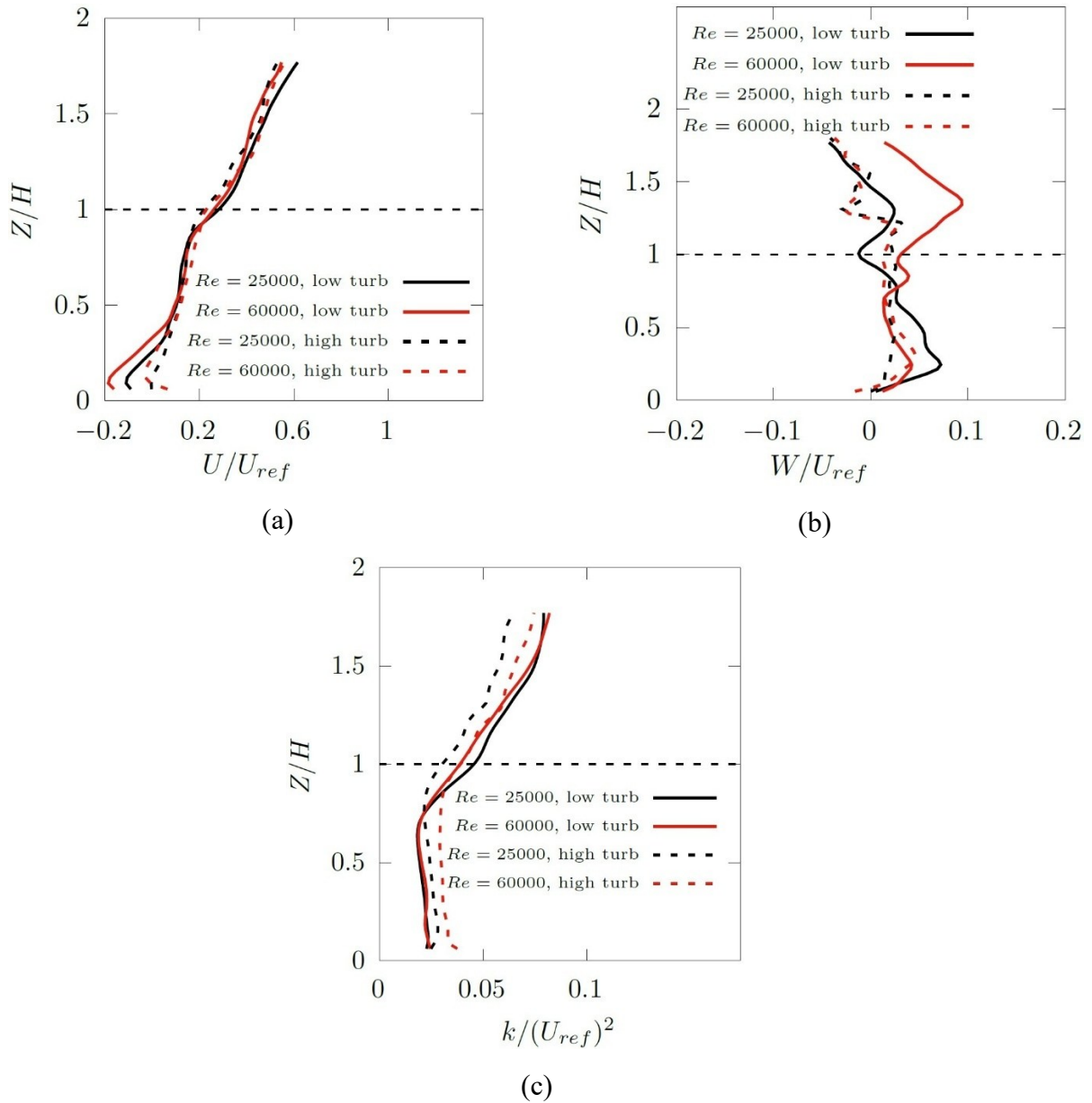


Figure 41. Profiles of the non-dimensional: (a) mean streamwise velocity (U/U_{ref}), (b) mean vertical velocity (W/U_{ref}) and (c) turbulent kinetic energy (k/U_{ref}^2) for the low and high (dashed lines) turbulence cases at $X/H = 0.5$ and $Y/H = 0$, with $U_{ref} = U_{\infty}$. Results are shown for the minimum and maximum Reynolds numbers tested in the wind tunnel of NTUA i.e. 25000 and 60000.

5 References

- [1] Meroney, R. N., Pavageau, M., Rafailidis, S. & Schatzmann, M. (1996). Study of line source characteristics for 2-D physical modelling of pollutant dispersion in street canyons. *Journal of wind Engineering and industrial Aerodynamics*, Volume 62(1), pp. 37-56.
- [2] Oke, T. R. (1988). Street design and urban canopy layer climate. *Energy and buildings*, 11(1-3), 103–113.
- [3] Dsouza, B., Sciacchitano, A. & Yu, W. (2024). Reynolds Number Independence In An Urban Street Canyon Using 3D Robotic Particle Tracking Velocimetry. *21st International Symposium on Applications of Laser and Imaging Techniques to Fluid Mechanics*, Lisbon, 08-11 July 2024.
- [4] Chew, L.W., Aliabadi, A. A., & Norford, L. K. (2018). Flows across high aspect ratio street canyons: Reynolds number independence revisited. *Environmental Fluid Mechanics*, 18, 1275–1291.
- [5] Shu, C., Wang, L. L., & Mortezaadeh, M. (2020). Dimensional analysis of Reynolds independence and regional critical Reynolds numbers for urban aerodynamics. *Journal of Wind Engineering and Industrial Aerodynamics*, 203, 104232.
- [6] Raffel, M., Willert, C. E., Scarano, F., Kähler, C. J., Wereley, S. T., & Kompenhans, J. (2018). Particle image velocimetry: a practical guide. *springer*.
- [7] Scarano, F. (2012). Tomographic PIV: principles and practice. *Measurement Science and Technology*, 24(1), 012001.
- [8] Schanz, D., Gesemann, S., & Schröder, A. (2016). Shake-The-Box: Lagrangian particle tracking at high particle image densities. *Experiments in fluids*, 57, 1-27.
- [9] Schanz D, Schröder A, Gesemann S, Michaelis D, & Wieneke B (2013) Shake-the-Box: a highly efficient and accurate tomographic particle tracking velocimetry (TOMO-PTV) method using prediction of particle position. *10th international symposium on particle image velocimetry—PIV13*. Delft, The Netherlands, 1–3 July 2013.
- [10] Wieneke, B. (2012). Iterative reconstruction of volumetric particle distribution. *Measurement Science and Technology*, 24(2), 024008.
- [11] Schröder A, Schanz D, Geisler R, Gesemann S, & Willert C (2015b). Near-wall turbulence characterization using 4D-PTV Shake-The-Box. *11th international symposium on particle image velocimetry—PIV15*. Santa Barbara, California, 14–16 Sept 2015.
- [12] Schneiders, J. F., Scarano, F., Jux, C., & Sciacchitano, A. (2018). Coaxial volumetric velocimetry. *Measurement Science and Technology*, 29(6), 065201.
- [13] Gromke, C., & Ruck, B. (2009). On the impact of trees on dispersion processes of traffic emissions in street canyons. *Boundary-Layer Meteorology*, 131, 19-34.
- [14] Musou Black, URL: <https://www.musoublack.com/>, accessed: 26.09.24.
- [15] Faleiros, D. E., Tuinstra, M., Sciacchitano, A., & Scarano, F. (2019). Generation and control of helium-filled soap bubbles for PIV. *Experiments in Fluids*, 60, 1–17.
- [16] Kim, D., Kim, M., Saredi, E., Scarano, F., & Kim, K. C. (2020). Robotic PTV study of the flow around automotive side-view mirror models. *Experimental Thermal and Fluid Science*, 119, 110202.
- [17] Pappa, V., Muehle, F., Tamaro, S., Campagnolo, F., Bottasso, C., Dsouza, B., Sciacchitano, A., Chasapogiannis, P., & Manolesos, M. (2024). Twin Test 2: Wake interactions of a cluster of turbines and wake steering techniques. URL: http://tweet-ie.eu/dp/results/33-TWEET-IED4.1BookofReference_TWT2_v3.pdf, accessed: 27.09.24.
- [18] Wieneke, B. (2008). Volume self-calibration for 3D particle image velocimetry. *Experiments in fluids*, 45(4), 549-556.
- [19] Schanz, D., Gesemann, S., Schröder, A., Wieneke, B., & Novara, M. (2012). Non-uniform optical transfer functions in particle imaging: calibration and application to tomographic reconstruction. *Measurement Science and Technology*, 24(2), 024009.



-
- [20] Pappa, V., Pallas, N.P., Bouris, D., Gromke, C., Riziotis, V., Manolesos, M., Prospathopoulos, J., Chasapogiannis, P., Kellaris, K., & Vassilopoulos, K. (2023). Twin Test 1: Effects of Vegetation on Flows in the Urban Environment URL: http://tweet-ie.eu/dp/results/27-TWEET-IED4.1BookofReference_TWT1_v1.1.pdf, accessed: 04.10.24.
- [21] Pappa, V., Bouris, D., Theurer, W., & Gromke, C. (2023). A wind tunnel study of aerodynamic effects of façade and roof greening on air exchange from a cubic building. *Building and Environment*, 231, 110023.
- [22] Chew, L. W., & Norford, L. K. (2018). Pedestrian-level wind speed enhancement in urban street canyons with void decks. *Building and Environment*, 146, 64-76.
- [23] Brochure with information about the open jet facility (OJF) located at TU Delft, URL: https://filelist.tudelft.nl/LR/Organisatie/Afdelingen/Aerodynamics__Wind_Energy__Flight_Performance_and_Propulsion/OJF_boek.pdf, accessed: 23.09.24.
- [24] Sciacchitano, A., & Wieneke, B. (2016). PIV uncertainty propagation. *Measurement Science and Technology*, 27(8), 084006
- [25] Schneiders, J. F., & Sciacchitano, A. (2017). Track benchmarking method for uncertainty quantification of particle tracking velocimetry interpolations. *Measurement Science and Technology*, 28(6), 065302.
- [26] Sciacchitano, A. (2019). Uncertainty quantification in particle image velocimetry. *Measurement Science and Technology*, 30(9), 092001.
- [27] Bhattacharya, S., & Vlachos, P. P. (2020). Volumetric particle tracking velocimetry (PTV) uncertainty quantification. *Experiments in Fluids*, 61, 1-18.

